Kinetic simulations of imbalanced turbulence in a relativistic plasma: Net flow and particle acceleration

Amelia M. Hankla [1,2]★† Vladimir Zhdankin,[3] Gregory R. Werner [4] Dmitri A. Uzdensky[4] and Mitchell C. Begelman[1,5]

[1]*JILA, University of Colorado and National Institute of Standards and Technology, 440 UCB, Boulder, CO 80309-0440, USA*
[2]*Department of Physics, University of Colorado, 390 UCB, Boulder, CO 80309-0390, USA*
[3]*Department of Astrophysical Sciences, Princeton University, 4 Ivy Lane, Princeton, NJ 08544, USA*
[4]*Center for Integrated Plasma Studies, Department of Physics, University of Colorado, 390 UCB, Boulder, CO 80309-0390, USA*
[5]*Department of Astrophysical and Planetary Sciences, University of Colorado, 391 UCB, Boulder, CO 80309, USA*

ABSTRACT

Turbulent high-energy astrophysical systems often feature asymmetric energy injection: for instance, Alfvén waves propagating from an accretion disc into its corona. Such systems are 'imbalanced': the energy fluxes parallel and antiparallel to the large-scale magnetic field are unequal. In the past, numerical studies of imbalanced turbulence have focused on the magnetohydrodynamic regime. In this study, we investigate externally driven imbalanced turbulence in a collision-less, ultrarelativistically hot, magnetized pair plasma using 3D particle-in-cell (PIC) simulations. We find that the injected electromagnetic momentum efficiently converts into plasma momentum, resulting in net motion along the background magnetic field with speeds up to a significant fraction of lightspeed. This discovery has important implications for the launching of accretion disc winds. We also find that although particle acceleration in imbalanced turbulence operates on a slower time-scale than in balanced turbulence, it ultimately produces a power-law energy distribution similar to balanced turbulence. Our results have ramifications for black hole accretion disc coronae, winds, and jets.

Key words: acceleration of particles – plasmas – relativistic processes – turbulence.

1 INTRODUCTION

High-energy astrophysical systems such as accretion discs, jets, and pulsar wind nebulae often comprise collision-less, relativistically hot plasmas and are likely turbulent (Shakura & Sunyaev 1973; Sparks, Biretta & Macchetto 1996; Balbus & Hawley 1998; Hester 2008). Turbulence in systems with magnetization (the ratio of magnetic enthalpy to plasma enthalpy) $\sigma \gtrsim 1$ can efficiently accelerate particles, as recently demonstrated in particle-in-cell (PIC) simulations (Zhdankin et al. 2017, 2018b; Comisso & Sironi 2018, 2019). Such non-thermal particle acceleration (NTPA) could explain the power laws seen in spectra of jets, pulsar wind nebulae, and stellar mass black hole X-ray binary systems (Remillard & McClintock 2006; Abdo et al. 2009; Aleksić et al. 2015).

These previous studies of turbulence in relativistic collision-less plasmas have assumed symmetric energy injection into the plasma. However, this assumption is not true in a variety of space and astrophysical systems where turbulence is preferentially stirred on one side of the system. For example, in an accretion disc–wind system, turbulence in the disc may shake the footpoint of an open large-scale magnetic field line, sending Alfvén waves predominately away from the disc's mid-plane and into the corona (Chandran, Foucart &

Tchekhovskoy 2018). This asymmetric propagation of Alfvén waves could impact NTPA. In addition, if efficiently coupled to the plasma, such asymmetrically injected electromagnetic momentum could result in bulk motion of the plasma – an outflow/wind. Understanding both NTPA and the possible formation of an outflow necessitates studying turbulence with asymmetric momentum injection – the so-called 'imbalanced' turbulence.

Most studies of imbalanced turbulence have focused on the magnetohydrodynamic (MHD) regime. Canonical phenomenological models for strong, 'balanced' MHD turbulence consider ensembles of counter-propagating Alfvén waves with equal energy fluxes along a background magnetic field (Iroshnikov 1964; Kraichnan 1965; Goldreich & Sridhar 1995; Thompson & Blaes 1998; Boldyrev 2006); see Schekochihin (2020) for a recent review. Phenomenological models for imbalanced turbulence relax the assumption of equal fluxes, leading to predictions that are ripe for numerical exploration (Lithwick, Goldreich & Sridhar 2007; Beresnyak & Lazarian 2008; Chandran 2008; Perez & Boldyrev 2009). Numerical attempts to model imbalanced turbulence in the MHD regime have proven difficult due to questions about the effects of varying dissipation prescriptions, limited dynamic ranges of accessible simulation domains, and limited run times (Beresnyak & Lazarian 2009, 2010; Perez & Boldyrev 2010a,b; Mason et al. 2012; Perez et al. 2012). Some numerical studies have extended beyond standard MHD to the relativistic MHD regime using the

★ E-mail: amelia.hankla@colorado.edu
† National Science Foundation Graduate Research Fellow.

force-free assumption that $\sigma \gg 1$ (Cho & Lazarian 2014; Kim & Cho 2015).

Below MHD scales, analytic models of imbalanced kinetic turbulence have recently been formulated in the non-relativistic regime (Voitenko & De Keyser 2016; Passot & Sulem 2019; Gogoberidze & Voitenko 2020). These models of collision-less imbalanced turbulence can be tested against measurements of the solar wind (Chen 2016). Meanwhile, numerical studies have made approximations of infinite ion-to-electron mass ratio to model scales below the proton gyroradius (Cho & Kim 2016), demonstrated the importance of finite Larmor radius effects on the turbulent energy cascade (Meyrand et al. 2021), or employed a diffusive model to study turbulence from fluid to sub-ion scales (Miloshevich, Passot & Sulem 2020). A few numerical studies have modelled the fully kinetic collision-less regime with an eye towards the solar wind (Grošelj et al. 2018). However, none to our knowledge have examined the ultrarelativistic, collision-less regime relevant to high-energy astrophysical systems. Studying this regime is important because quasi-linear models of turbulent particle acceleration for imbalanced MHD predict a decrease in the Fokker–Planck momentum diffusion coefficient for increasing imbalance, leading to less efficient NTPA and posing a potential obstacle to turbulence as an astrophysical particle accelerator in some systems (Schlickeiser 1989; Chandran 2000).

In this work, we explore imbalanced, relativistic turbulence in magnetized collision-less electron–positron (pair) plasmas using 3D PIC methods (Zhdankin et al. 2018a). We study how imbalance affects self-consistent NTPA, inaccessible in fluid-based models, and how it introduces an effect entirely absent in balanced models: the transfer of net momentum to the plasma, which in realistic systems could form outflows. Though the regime we simulate is particularly applicable to black hole accretion disc coronal heating (Chandran et al. 2018) and wind-launching, our results should be generally applicable to relativistic astrophysical turbulence where the source of perturbations is localized, such as the jets originating from active galactic nuclei.

To frame our study of this numerically and analytically unexplored regime of turbulence, we focus on four main questions:

(i) How does imbalance affect the formation of a turbulent cascade?

(ii) How does imbalance affect the partition of large-scale injected energy into electromagnetic, internal, and turbulent kinetic energy?

(iii) Does imbalance drive net motion of the plasma?

(iv) How does imbalance affect NTPA?

We first introduce the numerical tools and parameters used to describe imbalanced turbulence (Section 2). We then present the results of 3D collision-less, relativistic PIC simulations with varying degrees of imbalance and ratio of system size to initial Larmor radius that address each of the above questions in order. After first demonstrating the presence of a turbulent cascade (Section 3.1), we discuss how and why the energy partition changes with imbalance (Section 3.2). Then we examine the formation of a net flow via efficient momentum transfer to the plasma and provide an analytic framework for understanding it (Section 3.3). We continue by demonstrating, for the first time, the similarity of NTPA in balanced and imbalanced turbulence (Section 3.4). We check the dependence of our results on simulation domain size in Appendix A. We conclude with implications for high-energy astrophysical systems and remaining questions (Section 4).

2 METHODS

In this section, we will first review physical properties of relativistic magnetized plasmas (Section 2.1), and then outline the simulation suite used to study imbalanced turbulence (Section 2.2). The last subsection discusses various diagnostics that will be used to analyse our simulations (Section 2.3).

2.1 Plasma physical regime

The plasmas considered in this paper are collision-less, ultrarelativistically hot, and magnetized. This section discusses the parameters that characterize such a plasma. Throughout this work, we will use $\langle \cdot \rangle$ to denote the time-dependent volume- or particle ensemble-average of a quantity and – to denote the time-average of a quantity in the time interval $10 < tc/L < 20$ unless otherwise specified; here L/c is the light-crossing time of the simulation domain with length L.

The parameters that characterize an ultrarelativistic, magnetized pair plasma with $\langle \gamma \rangle \gg 1$ include: an average total (electron plus positron) particle density n_0, average particle energy $\langle \gamma \rangle m_e c^2$, and characteristic magnetic field strength $B_{\rm rms} = \sqrt{\langle B_x^2 + B_y^2 + B_z^2 \rangle}$. Here, m_e is the mass of the electron (or positron) and $\langle \gamma \rangle$ is the average particle Lorentz factor ($\gamma = 1/\sqrt{1 - v^2/c^2} = \sqrt{1 + p^2/m_e^2 c^2}$ for a particle with velocity v, mass m_e, and momentum p). The fundamental physical length scales in this plasma are: the characteristic Larmor radius $\rho_e = \langle \gamma \rangle m_e c^2/eB_{\rm rms}$, the plasma skin depth $d_e = (\langle \gamma \rangle m_e c^2/(4\pi n_0 e^2))^{1/2}$, and the size of the system L. For a plasma with a Maxwell–Jüttner particle distribution $f(\gamma) = \gamma^2 \sqrt{1 - 1/\gamma^2} \, [\theta K_2(1/\theta)]^{-1} \exp(-\gamma/\theta)$, the plasma has a well-defined temperature $T_e = \langle \gamma \rangle m_e c^2/3$ (assumed equal for electrons and positrons) and the Debye length simplifies to $\lambda_D = d_e/\sqrt{3}$. Here $\theta \equiv T_e/m_e c^2$ and $K_2(x)$ is the modified Bessel function of the second kind. The three length scales ρ_e, d_e, and L form two dimensionless quantities: the magnetization $\sigma = B_{\rm rms}^2/4\pi h = 3(d_e/\rho_e)^2/4$ and the ratio of the largest characteristic scale of spatial variation $L/2\pi$ (which will be the turbulence driving scale in our study as described below) to the Larmor radius ρ_e. Here $h = n_0\langle \gamma \rangle m_e c^2 + \langle P \rangle \approx 4n_0\langle \gamma \rangle m_e c^2/3$ is the characteristic relativistic enthalpy density and $\langle P \rangle \approx n_0\langle \gamma \rangle m_e c^2/3$ is the (assumed isotropic) average plasma pressure. The magnetization is related to the plasma beta parameter $\beta = 8\pi \langle P \rangle/B_{\rm rms}^2$ as $\beta = 1/(2\sigma)$ and determines the relativistic Alfvén speed $v_A = c\sqrt{\sigma/(\sigma + 1)}$. Since we consider primarily Alfvénic turbulence, the magnetization governs how relativistic the large-scale turbulent motion is.

2.2 Numerical simulations

To explore the properties of imbalanced turbulence in a collision-less relativistic pair plasma from first principles, we use the electromagnetic PIC code ZELTRON (Cerutti et al. 2013). ZELTRON samples the particle phase space with macroparticles and evolves them according to the Lorentz force law, providing an approximate solution to the relativistic Vlasov equation. The electric and magnetic fields evolve according to Maxwell's equations, with the addition of an externally driven volumetric current to Ampère's law to generate turbulence, as discussed below.

The physical parameters of the simulations we present are identical to those described in Zhdankin et al. (2018a, b) except for the modifications outlined below to introduce imbalance. Each simulation is initialized with an electron–positron plasma at rest with a Maxwell–Jüttner distribution function, a uniform background magnetic field $\boldsymbol{B}_0 = B_0 \hat{z}$ and no initial electromagnetic fluctuations.

For each of the simulations, we set the initial magnetization to $\sigma_0 = 0.5$, yielding a relativistic Alfvén velocity $v_{A0} = 0.58c$ and plasma beta $\beta_0 = 1.0$. The initial temperature of the plasma is fixed at $T_e = 100 m_e c^2$ across all simulations, corresponding to an initial average particle Lorentz factor of $\langle \gamma \rangle \approx 300$.

To obtain the largest possible inertial range, the simulation suite's chosen numerical parameters maximize the separation between the large driving scale $L/2\pi$ and the small initial kinetic scales ρ_{e0} and d_{e0}, while still resolving the latter. We resolve the initial plasma length scales with fixed $\Delta x = \rho_{e0}/1.5 = d_{e0}/1.22$, where $\Delta x = \Delta y = \Delta z$ is the grid cell length in each direction. The simulation domain is cubic with periodic boundary conditions and length $L \equiv N\Delta x$, where N is the number of cells in a spatial dimension (throughout, $N_x = N_y = N_z \equiv N$). The time-step is a fraction of the cell light-crossing time, i.e. $\Delta t = 3^{-1/2}\Delta x/c$. The simulations are initialized with 32 particles per cell per species. To scan the ratio $L/2\pi \rho_{e0}$, we vary the number of cells in each spatial dimension, with $N = 256, 384, 512,$ and 768 corresponding to $L/2\pi \rho_{e0} \in \{27.1, 40.7, 54.3, 81.5\}$. When examining the dependence of results on simulation size, we also include three simulations of balanced turbulence with $L/2\pi \rho_{e0} \in \{81.5, 108.7, 164\}$ ($N \in \{768, 1024, 1536\}$) used in Zhdankin et al. (2018b) that are otherwise identical to the simulations presented in this work.

The initial equilibrium is disrupted by an externally driven current. We employ an oscillating Langevin antenna (OLA; TenBarge et al. 2014) to drive turbulence volumetrically and continually throughout each simulation's duration. The OLA is implemented by adding the external current to the evolution equation for the electric field (Ampère's law). This current generates counter-propagating Alfvén waves. The amplitudes of these counter-propagating waves are modified to induce imbalanced turbulence, as described in the following paragraphs. Because of the random nature of the OLA driving, a single simulation may not be representative of the entire ensemble of possible random seeds. To avoid basing all our conclusions on a single data point for each balance parameter, we also present a statistical study of random seeds. For each balance parameter, eight values of the random seed are simulated for the domain size $L/2\pi \rho_{e0} = 40.7$ ($N = 384$). The results of the statistical study are compared against the largest simulation domains $L/2\pi \rho_{e0} = 81.5$ ($N = 768$). Statistical variation could potentially be reduced in a single simulation by introducing more than eight driving modes.

We drive imbalanced turbulence via eight independently evolved, externally driven sinusoidal current modes. These current modes create magnetic field perturbations propagating in opposite directions along the background magnetic field, i.e. Alfvén waves. The driven current modes have the form:

$$J_x^{\text{ext}}(\boldsymbol{x}, t) = \frac{2\pi c}{L^2} \text{Re} \left[\sum_{j=1}^{2} \left(a_j(t) e^{i \boldsymbol{k}_j \cdot \boldsymbol{x}} + b_j(t) e^{-i \boldsymbol{k}_j \cdot \boldsymbol{x}} \right) \right] \quad (1)$$

$$J_y^{\text{ext}}(\boldsymbol{x}, t) = \frac{2\pi c}{L^2} \text{Re} \left[\sum_{j=3}^{4} \left(a_j(t) e^{i \boldsymbol{k}_j \cdot \boldsymbol{x}} + b_j(t) e^{-i \boldsymbol{k}_j \cdot \boldsymbol{x}} \right) \right] \quad (2)$$

$$J_z^{\text{ext}}(\boldsymbol{x}, t) = \frac{2\pi c}{L^2} \text{Re} \left[\sum_{j=1}^{4} \left(-a_j(t) e^{i \boldsymbol{k}_j \cdot \boldsymbol{x}} + b_j(t) e^{-i \boldsymbol{k}_j \cdot \boldsymbol{x}} \right) \right]. \quad (3)$$

The sign of k_z dictates the direction of the current mode's propagation. Four of the modes have no y-component of their wavevector and four have no x-component; four propagate in the $+z$-direction and four propagate in the $-z$-direction. These wavevectors are

$$\boldsymbol{k}_1 = k_0(-1, 0, 1) \quad \boldsymbol{k}_2 = k_0(1, 0, 1) \quad (4)$$

$$\boldsymbol{k}_3 = k_0(0, -1, 1) \quad \boldsymbol{k}_4 = k_0(0, 1, 1). \quad (5)$$

Here, $k_0 = 2\pi/L$, so that the driving scale is the largest scale $L/2\pi$. We ensure $\nabla \cdot \boldsymbol{J}_{\text{ext}} = 0$ to avoid local injection of net charge. Currents driven in $J_{\text{ext},x}$ and $J_{\text{ext},y}$ create Alfvén waves with magnetic field perturbations in the y- and x-directions, respectively. The amplitudes of these currents can be adjusted to create counter-propagating Alfvén waves of unequal amplitudes, thus enabling our study of imbalanced turbulence.

The external current's time-dependence is dictated by the coefficients $a_j(t)$ and $b_j(t)$. The coefficient at the $(n+1)$th time-step is found from the previous nth time-step as

$$a_j^{(n+1)} = a_j^{(n)} e^{-i\omega\Delta t} + \alpha_j u_j^{(n)} \Delta t \quad (6)$$

$$b_j^{(n+1)} = b_j^{(n)} e^{-i\omega\Delta t} + \beta_j v_j^{(n)} \Delta t. \quad (7)$$

The coefficients $a_j(t)$ and $b_j(t)$ thus oscillate at frequency ω with random kicks at each time-step (cf. Langevin equation, hence the name 'oscillating Langevin antenna'; TenBarge et al. 2014). The initial coefficients $a_j^{(0)}$ and $b_j^{(0)}$ are set to amplitudes $\mathcal{A}$ and $\mathcal{B}$ multiplied by random phases $\phi_j^{(a)}$ and $\phi_j^{(b)}$: $a_j^{(0)} = \mathcal{A}e^{i\phi_j^{(a)}}$ and $b_j^{(0)} = \mathcal{B}e^{i\phi_j^{(b)}}$. We set $\mathcal{A} = B_0 L/8\pi$, which for balanced turbulence achieves $\delta B_{\text{rms}} = \sqrt{B_{\text{rms}}^2 - B_0^2} \sim B_0$. The random kicks $u_j^{(n)}$ and $v_j^{(n)}$ in equations (6) and (7) are complex random numbers with real and imaginary components drawn from a uniform distribution between -0.5 and 0.5. The constant parameters α_j and β_j are set such that when ensemble-averaged, $\langle |a_j^{(n)}|^2 \rangle = \mathcal{A}^2$ and $\langle |b_j^{(n)}|^2 \rangle = \mathcal{B}^2$. The complex driving frequency ω has real component ω_0 and an imaginary component $-\Gamma_0$ which we set to be non-integer multiples of the Alfvén frequency $\omega_A \equiv 2\pi v_A/L$ to avoid initial resonances: $\omega_0 = (0.6/\sqrt{3})\omega_A \approx 0.35\omega_A$ and $\Gamma_0 = (0.5/\sqrt{3})\omega_A \approx 0.29\omega_A$. In frequency space, the driving is a Lorentzian centered at ω_0 with a full-width half-max of Γ_0; see TenBarge et al. (2014) for details. The amplitudes $\mathcal{A}$ and $\mathcal{B}$ (and therefore the α_j and β_j values) are the same for all a_j and b_j, but the random parameters u_j, v_j, and the initial phases $\phi_j^{(a,b)}$ are different for each k_j.

We introduce imbalance by adjusting the amplitudes of the currents propagating in the $-z$-direction relative to those propagating in the $+z$-direction. The coefficients a_j control the currents propagating in the $+z$-direction, whereas b_j control the waves propagating in the $-z$-direction. These currents' amplitudes are dictated by their respective $\mathcal{A}$ and $\mathcal{B}$ amplitudes. To achieve imbalanced turbulence, we hold $\mathcal{A}$ fixed and vary $\mathcal{B}$. We quantify how balanced the turbulence is via the balance parameter,

$$\xi \equiv \mathcal{B}/\mathcal{A}, \quad (8)$$

where $\mathcal{B}$ is the amplitude for the $-z$-modes and $\mathcal{A}$ is the fixed amplitude for the $+z$-modes. A value of $\xi = 1$ corresponds to the canonical balanced case, whereas $\xi = 0$ corresponds to current modes propagating only in the $+z$-direction. Because we drive currents rather than Alfvén modes, we do not directly control the exact amplitude of counter-propagating Alfvén waves. If $\xi = 0$ corresponded exactly to the case of Alfvén waves propagating in a single direction, we would not expect turbulence to develop in a non-relativistic, ideal MHD plasma. Indeed, turning off the random kicks by setting $\alpha_j = \beta_j = 0$ does not result in turbulence for simulations with $\xi = 0$ (not shown). However, with our set-up of non-zero α_j and β_j, the $\xi = 0$ case does become turbulent because the OLA forcing excites counter-propagating Alfvén waves. In principle, more imbalanced turbulence should be achievable by, e.g. a decaying

Table 1. Measured values of the Elsasser fields' energy ratio $r_E = \langle \overline{z_-^2} \rangle / \langle \overline{z_+^2} \rangle$ for a sampling of balance parameter ξ values. The first number gives the ratio for $N = 768$ and the second gives one standard deviation of the $N = 384$ statistical seed studies. Time averages are taken over $5.0 < tc/L < 20.0$.

ξ	0.0	0.5	1.0
r_E	0.72 ± 0.06	0.92 ± 0.14	1.01 ± 0.14

turbulence problem or by changing the driving mechanism. For this work, we simply term the $\xi = 0$ case the 'most imbalanced' case.

We will use the balance parameter ξ throughout this paper to refer to the degree of imbalance; however, since ξ measures the imbalance of the driving mechanism rather than the turbulence, we now briefly discuss the relationship of ξ to other methods of measuring imbalance. Cross-helicity, an invariant in ideal MHD, measures the difference in the energy densities associated with waves propagating antiparallel (with energy density $\mathcal{E}_+$ and amplitude δB_+) and parallel to the magnetic field (with energy density $\mathcal{E}_-$ and amplitude δB_-). In ideal, non-relativistic, incompressible MHD, $\mathcal{E}_\pm = \langle \rho |z_\pm|^2 \rangle / 4$, where $z_\pm = \delta v \pm b$ are the Elsasser fields (Elsasser 1950). Here δv is the fluctuating plasma velocity, $b \equiv \delta B \; v_A/B_0$ is the fluctuating magnetic field in velocity units, and ρ is the plasma mass density (not to be confused with the Larmor radius ρ_e). The total energy density is then given by $\mathcal{E} \equiv \mathcal{E}_+ + \mathcal{E}_- = (1/2)\langle \rho \left(|\delta v|^2 + |b|^2 \right) \rangle$ and the cross-helicity $H_c \equiv (\mathcal{E}_+ - \mathcal{E}_-)/\langle \rho \rangle$ can be re-expressed as $H_c = \langle \delta v \cdot b \rangle$. Cross-helicity is related to the volume-averaged z-component of the Poynting flux $S(x, t) = (c/4\pi)[E \times B]$ under the assumptions of incompressible, non-relativistic, ideal reduced MHD that $\delta B \ll B_0$ and that the fluctuations δB and δv are perpendicular to the background field $B_0 \hat{z}$:

$$\langle S_z \rangle(t) = -\frac{B_0}{4\pi}\langle \delta v \cdot \delta B \rangle = -\frac{1}{4\pi}\frac{B_0^2}{v_A} H_c(t). \tag{9}$$

For a single Alfvén wave, $\delta v/v_A = \pm \delta B/B_0$ and thus the magnitude of the Poynting flux for a single Alfvén wave $|\langle S_z \rangle_{1-\text{wave}}|$ is

$$|\langle S_z \rangle_{1-\text{wave}}| = \frac{1}{4\pi}\langle \delta B^2 \rangle v_A. \tag{10}$$

We can estimate the values of the driven Alfvén wave energies in our simulations of imbalanced turbulence as $E_+ \sim \langle \delta B_+^2 \rangle \sim |a_j|^2$ (where δB_+ is the amplitude of the magnetic perturbation travelling in the $+z$ direction) and $E_- \sim |b_j|^2$, leading to

$$\langle S_z \rangle \propto H_c \propto 1 - \xi^2. \tag{11}$$

Equation (11) will be tested in Section 3.3.2. Normalizing to the total energy, the 'normalized cross-helicity' $\tilde{H}_c = (\mathcal{E}_+ - \mathcal{E}_-)/(\mathcal{E}_+ + \mathcal{E}_-)$ (Perez & Boldyrev 2009; Chen 2016; Meyrand et al. 2021) can be estimated as $\tilde{H}_c \sim (1 - \xi^2)/(1 + \xi^2)$. Finally, we calculate the ratio $\langle \overline{z_-^2} \rangle / \langle \overline{z_+^2} \rangle$ of Elsasser field energies for several ξ (Table 1). These fields are calculated with $v_A(t) = c\sqrt{\sigma(t)/(\sigma(t) + 1)}$ using the instantaneous magnetization. For our most imbalanced turbulence ($\xi = 0.0$), the ratio of energies is about 0.72, whereas for perfectly imbalanced turbulence the ratio would be zero. The discrepancy between the driving's imbalance and the turbulence's imbalance is due to the excitation of counter-propagating Alfvén waves (discussed in the previous paragraph), and possibly relativistic, kinetic, and moving frame effects, which the Elsasser fields we use do not take into account.

The main goal of our study is to determine the impact of imbalance on the properties of collision-less turbulence. We do so by varying

the balance parameter ξ between 0 ('most imbalanced') and 1 ('balanced') at every value of $L/2\pi \rho_{e0}$.

2.3 Energy diagnostics

In this section, we discuss diagnostics that will be used in Section 3 to partition the energy of the system into four main types.

The total energy density in the system can be decomposed into the energy density $\mathcal{E}_{EM}$ in the electric and magnetic fields and the total (kinetic plus rest mass) energy density $\mathcal{E}_{pl}$ in the plasma particles. Fluid quantities provide intuition into the plasma's behaviour by partitioning $\mathcal{E}_{pl}$ into internal, net flow, and turbulent flows:

$$\mathcal{E}_{pl}(x, t) = \mathcal{E}_{int}(x, t) + \mathcal{E}_{net}(t) + \mathcal{E}_{turb}(x, t). \tag{12}$$

The plasma's total kinetic, internal, and turbulent kinetic energy densities are calculated for each simulation cell from both the electron and positron macroparticles' positions and momenta, though they will often be discussed in terms of their volume averages $\langle \mathcal{E}_{pl} \rangle$, $\langle \mathcal{E}_{int} \rangle$, and $\langle \mathcal{E}_{turb} \rangle$, respectively. The net flow energy density $\mathcal{E}_{net}$ is a key quantity for characterizing how efficiently imbalanced turbulence can drive a directed plasma flow. It is a global quantity calculated from the total momentum in the system. Explicitly, these quantities are defined as:

$$\mathcal{E}_{int}(x, t) \equiv \sqrt{\mathcal{E}_{pl}^2(x, t) - \mathcal{P}_{pl}^2(x, t)c^2} \tag{13}$$

$$\mathcal{E}_{net}(t) \equiv \langle \mathcal{E}_{pl} \rangle(t) - \sqrt{\langle \mathcal{E}_{pl} \rangle^2(t) - \langle \mathcal{P}_{pl} \rangle^2(t)c^2} \tag{14}$$

$$\mathcal{E}_{turb}(x, t) \equiv \mathcal{E}_{flow}(x, t) - \mathcal{E}_{net}(t), \tag{15}$$

where $\mathcal{E}_{flow}(x, t) = \mathcal{E}_{pl}(x, t) - \mathcal{E}_{int}(x, t)$ (equation 8, Zhdankin et al. 2018a) and $\mathcal{P}_{pl}(x, t)$ is the local momentum density of the electron–positron plasma. This framework is similar to that in Zhdankin et al. (2018a), with the renaming of the 'bulk' energy density to the 'flow' kinetic energy density and further breakdown of the flow energy density into the energy density associated with the net flow of the plasma $\mathcal{E}_{net}$ through the simulation domain and the turbulent motions $\mathcal{E}_{turb}$. Equation (13) for the internal energy density is analogous to the relativistic energy E of a single particle $E^2 = (mc^2)^2 + p^2c^2$. In this analogy, the plasma internal energy acts like a particle rest mass, the plasma momentum acts as a particle momentum, and the total plasma kinetic energy acts like a relativistic particle mass. Equation (14) for the net flow energy density uses a similar analogy, specifically applied to the quantity volume-averages.

The change in the energy of the plasma and the electromagnetic fields comes from the energy injected into the system by the OLA driving. The energy injection rate $\langle \dot{\mathcal{E}}_{inj} \rangle = -\langle J_{ext} \cdot E \rangle$ is statistically constant in time. Integrating it over time gives the total injected energy density up to time t: $\mathcal{E}_{inj}(t)$. Because the injected energy depends on the amplitude of the driven waves, its value at any given time varies with ξ within a factor of two or so (see Section 3.2). To account for this dependence of injected energy on balance parameter, we normalize the volume-averaged changes in the various energy components by the volume-averaged injected energy to obtain energy efficiencies:

$$1 = \frac{\Delta\langle \mathcal{E}_{int} \rangle}{\langle \mathcal{E}_{inj} \rangle} + \frac{\Delta\langle \mathcal{E}_{net} \rangle}{\langle \mathcal{E}_{inj} \rangle} + \frac{\Delta\langle \mathcal{E}_{turb} \rangle}{\langle \mathcal{E}_{inj} \rangle} + \frac{\Delta\langle \mathcal{E}_{EM} \rangle}{\langle \mathcal{E}_{inj} \rangle}, \tag{16}$$

where the terms on the right are the internal efficiency, net flow efficiency, turbulent kinetic efficiency, and electromagnetic efficiency, respectively. We use $\Delta\mathcal{E}$ to indicate the change in a type of energy density since the start of the simulation, i.e. $\Delta\mathcal{E}(t) = \mathcal{E}(t) - \mathcal{E}(0)$.
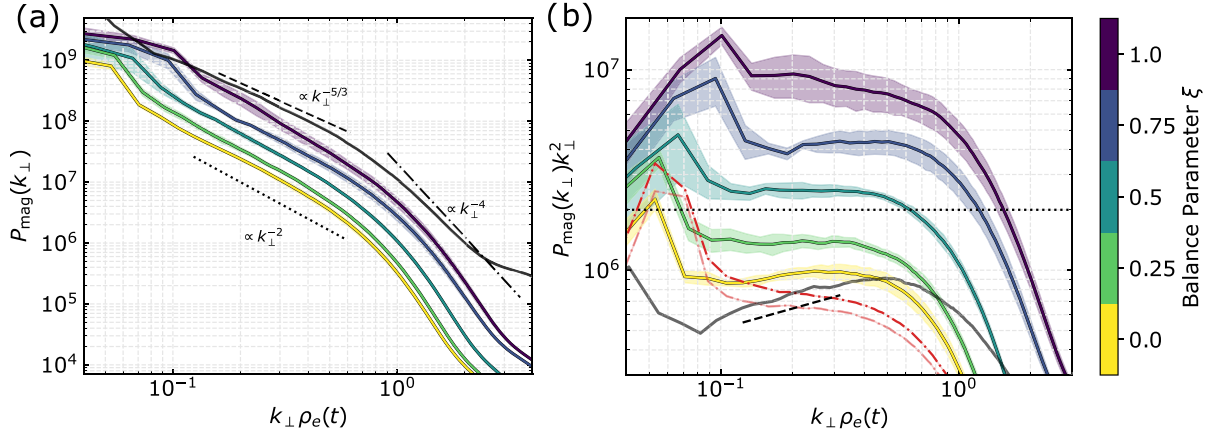
Figure 1. A turbulent cascade forms for all balance parameters. (a) The magnetic energy spectra $P_{\mathrm{mag}}(k_\perp)$ for $L/2\pi\rho_{e0} = 81.5$ simulations of varying balance parameter averaged between times $8.8 < tc/L < 9.9$ (comprising five outputs) show an inertial range between $k_\perp\rho_e(t) \sim 0.1$ and 1.0. A break in the spectrum at $k_\perp\rho_e(t) \sim 1.0$ indicates the onset of kinetic effects. (b) When compensated by $k_\perp^2$, the spectra for the balanced $\xi = 0.75$ and 1.0 cases are slightly steeper than $\propto k_\perp^{-2}$, whereas the imbalanced case $\xi = 0.0$ is slightly flatter. The Elsasser fields' spectra, shown in dash-dot red lines for $\xi = 0$, exhibit slightly different slopes, with the stronger field (z_+, top line) being slightly steeper than the weaker field (z_-, bottom line). In both panels, shaded lines show one temporal standard deviation about the mean. The black dashed lines show the scaling $k_\perp^{-5/3}$; black dotted lines show $k_\perp^{-2}$. The grey lines show the $L/2\pi\rho_{e0} = 164$ balanced simulation's magnetic energy spectrum, taken at $t = 8.9\,L/c$.

3 RESULTS

In this section, we investigate how imbalanced turbulence differs from balanced turbulence through a series of comparisons. After demonstrating the presence of a turbulent cascade for all values of balance parameter (Section 3.1), we examine how the injected energy transforms into the plasma's internal and turbulent energy (Section 3.2). We next turn to the novel aspect of imbalanced turbulence: the presence of a net flow (Section 3.3). By using the statistical study of eight random seeds at smaller simulation domains $L/2\pi\rho_{e0} = 40.7$ to enhance the trends in the largest simulation domains $L/2\pi\rho_{e0} = 81.5$, we constrain the dependence of each of these energy types on balance parameter. We then explore the decomposition of the plasma energy into thermal and non-thermal components and how particle acceleration depends on the balance parameter (Section 3.4). The influence of simulation domain size on the fluid quantities is explored by varying $L/2\pi\rho_{e0}$ in Appendix A.

3.1 Formation of a turbulent cascade

The spectrum of the turbulent magnetic energy is a common diagnostic when examining turbulence. Much of the previous work on imbalanced turbulence in MHD plasmas has examined the power-law indices of the two Elsasser fields and how they may or may not deviate from Goldreich-Sridhar $k_\perp^{-5/3}$ scalings (Goldreich & Sridhar 1995; Lithwick et al. 2007; Beresnyak & Lazarian 2008). In this study, we simply calculate the overall turbulent magnetic energy spectrum via:

$$P_{\mathrm{mag}}(k_\perp, t) = \int \mathrm{d}k_z \mathrm{d}\phi\, k_\perp\, \frac{1}{8\pi}(|\tilde{B}_x|^2 + |\tilde{B}_y|^2 + |\delta\tilde{B}_z|^2), \qquad (17)$$

where $\delta B_z = B_z - B_0$, k_z are the parallel wavenumbers, ϕ are the azimuthal angles, and $\tilde{\ }$ indicates the Fourier transform.

We find that the magnetic energy spectrum shows the formation of a turbulent cascade for all balance parameters (Fig. 1a). The spectra averaged over the time interval $8.8 < tc/L < 9.9$ (corresponding to $5.1 < tv_{A0}/L < 5.7$), i.e. after the turbulent cascade has fully developed but before the plasma's heating has diminished the inertial range, show similar shapes for all values of the balance parameter. The inertial

range forms between $k_\perp\rho_e(t) \sim 0.08$ and 0.6 for the most imbalanced case; a slightly shifted inertial range beginning at $k_\perp\rho_e(t) \sim 0.15$ rather than $k_\perp\rho_e(t) \sim 0.08$ for the simulations with more balanced turbulence ($\xi = 1.0$ and 0.75) results from the faster heating at these balance parameters. The power-law index in the inertial range is roughly consistent with $-5/3$, the classic MHD prediction for strong turbulence (Goldreich & Sridhar 1995). Although the magnetic energy spectrum better matches the $k_\perp^{-2}$ scaling characteristic of weak turbulence in the non-relativistic (Galtier et al. 2000) and relativistic (Ripperda et al. 2021; TenBarge et al. 2021) regimes, the turbulence in our simulations is strong. The steeper than 5/3 spectrum is likely due to a small domain size, as found by Zhdankin et al. (2018a). Identical balanced simulations with twice the domain size are consistent with a power-law index of $-5/3$ (dark grey line in Fig. 1a). Accurately measuring the power-law indices of imbalanced turbulence via larger domain sizes is beyond the scope of this study. Below the characteristic Larmor radius ($k_\perp\rho_e \gtrsim 1$), the spectrum steepens to another power law that covers a more limited range between $k_\perp\rho_e(t) \sim 1$ and 2 and is broadly consistent with the formation of a kinetic cascade with a power-law index of -4 for all values of imbalance (also found in Zhdankin et al. 2018a), much steeper than in the inertial range. Again, however, providing more exact values to test against the predictions and measurements in Schekochihin et al. (2009) or Zhdankin et al. (2018a) would require larger, better-resolved simulation domains. Numerical noise dominates at scales smaller than $k_\perp\rho_e(t) \sim 2$.

Although determining the precise dependence of the inertial range's slope on balance parameter would require a larger inertial range, there are hints that the slope depends on ξ. When the magnetic energy spectrum is compensated by the scaling $k_\perp^{-2}$, the simulation with balanced turbulence ($\xi = 1.0$) has a downward-sloping spectrum, whereas the simulation of turbulence with $\xi = 0$ has a slightly positive slope (Fig. 1b). However, this steepening is most likely due to increased damping. The balanced simulations heat up faster (as discussed in Section 3.2), resulting in smaller values of L/ρ_e than the imbalanced simulations. Due to the small domain sizes, our simulations cannot distinguish differences in slope caused by imbalance or dissipation.
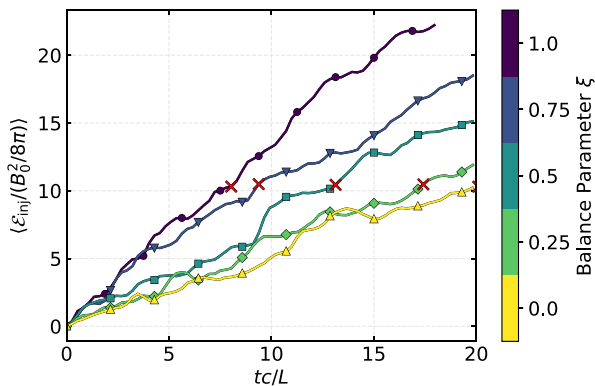
Figure 2. The amount of energy injected into a simulation depends on its balance parameter. The simulations of more balanced turbulence (purple and blue) have more injected energy than the simulations of less balanced turbulence (yellow and green). Red ×'s indicate the 'equivalent' times where the same amount of energy has been injected for each simulation (see Table 3), which all have $L/2\pi\rho_{e0} = 81.5$.

Because previous MHD predictions for imbalanced turbulence generally discuss the spectra of the Elsasser fields rather than the magnetic energy spectra, we also plot the Elsasser fields' spectra for the $\xi = 0$ case (dash-dot red lines in Fig. 1b). The larger amplitude field appears to have a slightly steeper slope than the smaller amplitude field, consistent with previous MHD simulations (Perez & Boldyrev 2010b; Perez et al. 2012). However, constraining the variation in the power-law index is difficult to quantify with such a short inertial range. If the dependence of the Elsasser fields' energy spectra on imbalance persists in larger simulations, it could support MHD predictions that the spectra's power-law indices depend on imbalance (Galtier et al. 2000; Chandran 2008).

Further evidence for the formation of a turbulent cascade comes from comparing the evolution of the energy injected into the simulation and the internal energy of the plasma. Whereas the accumulated injected energy increases linearly from $t = 0$ onward (Fig. 2), the internal energy density does not begin to increase until about 2.5 L/c, close to one Alfvén-crossing time (see Section 3.2.3, Fig. 3c). Presumably the energy injected at the driving scale cascades to smaller scales over the time period $t = 0-2.5\ L/c$ until it reaches the characteristic Larmor radius and dissipates into internal energy – i.e. the turbulent cascade forms in the first couple of light-crossing times. There appears to be an increase in the cascade formation time for decreasing balance parameter (see Section 3.2.3).

3.2 Partition of the injected energy

3.2.1 Framework for the energy partition

Because we drive the plasma in each simulation without an energy sink, the overall energy of each case increases in time. By adding a statistically constant amount of energy at each time-step, the overall amount of injected energy increases linearly in time (Fig. 2). The amplitude of the driven waves by definition depends on the balance parameter ξ (equation 8), and so the amount of energy injected also depends on ξ. The increase in injected energy is twice as fast for the balanced case $\xi = 1.0$ as for the most imbalanced case $\xi = 0.0$ (Fig. 2). This doubling of injected energy occurs because twice as many modes are driven in the balanced as in the most imbalanced case.

The injected energy converts into various types of plasma energy, each of which will be discussed in the following subsections. Fig. 3 shows temporal evolution of each quantity's energy density (left-hand panel) and energy efficiency (right-hand panel). The large-scale injected energy cascades to smaller scales in the form of bulk kinetic and electromagnetic energy until it is dissipated into internal energy, thereby implying that the internal energy should increase linearly in time during the statistical steady state – and it does, as shown in Fig. 3(c). As stationary conduits for the turbulent Alfvénic cascade, we expect both the turbulent kinetic and magnetic perturbations to fluctuate around steady-state values rather than continually increasing over time. Simulations support this idea of statistically steady-state values: the turbulent electromagnetic and kinetic energies saturate to their mean values around 7.5 L/c and fluctuate thereafter around these values (Figs 3 a and b). These values' dependence on balance parameter will be explored in Section 3.2.2, while the dependence of the internal energy density's slope on balance parameter is discussed in Section 3.2.3. The final component of plasma energy, the kinetic energy of net motion through the simulation domain, does not have an easily characterized evolution (Fig. 3d); its dependence on balance parameter will be discussed in Section 3.3.2.

Normalizing the change in each type of energy to the injected energy (the energy efficiency; equation 16) allows direct comparison between turbulence with different balance parameters while accounting for the injected energy's dependence on ξ (Fig. 4). By the end of the simulations at $t = 20\ L/c$, the percentage of injected energy that dissipates into internal energy depends on balance parameter, varying from ≈80 per cent for the most imbalanced case ($\xi = 0$) to ≈90 per cent for the balanced ($\xi = 1$) case. For all balance parameters, this percentage increases over time as the majority of injected energy converts into internal energy. In contrast, the fractions of injected energy that convert into turbulent electromagnetic and kinetic energy (i.e. the electromagnetic and kinetic energy efficiencies) decrease in time as $1/t$, plotted as dashed black lines in Fig. 4, with similar magnitudes for the balanced ($\xi = 1.0$) and most imbalanced ($\xi = 0.0$) case. These fits are motivated by the discussion in the previous paragraph; when normalized to the injected energy $\propto t$, these two types of turbulent energy can be fit to the function $A + B/t$. The fraction of injected energy that converts into net flow energy differs by an order of magnitude between the balanced case (1 per cent) and the imbalanced case (10 per cent). In both cases, however, the net flow efficiency remains relatively constant in time, indicating that a constant fraction of injected energy converts into net flow energy, with a clear dependence on ξ (also seen in Fig. 3h).

With a broad framework for the temporal evolution of internal, turbulent kinetic, and magnetic energy in hand, the following sections will explore each type of energy's dependence on balance parameter using various averages and highlighting statistical variation with the random seed study.

3.2.2 Electromagnetic and turbulent kinetic energy

After an initial transient period, the turbulent electromagnetic and kinetic energies become statistically constant in time (Figs 3a and b). The turbulent electromagnetic energy increases until it contains approximately the same amount of energy as in the background field (Fig. 3a). As ξ increases from 0 to 1, $\langle\overline{\Delta\mathcal{E}_{mag}}\rangle$ increases by about 50 per cent for turbulence in the largest simulation domain sizes (Fig. 5a). In contrast, the electric energy density decreases from 10 to 25 per cent of $B_0^2/8\pi$ for $\xi = 0.0$ to 10–17 per cent for $\xi = 1.0$ (not
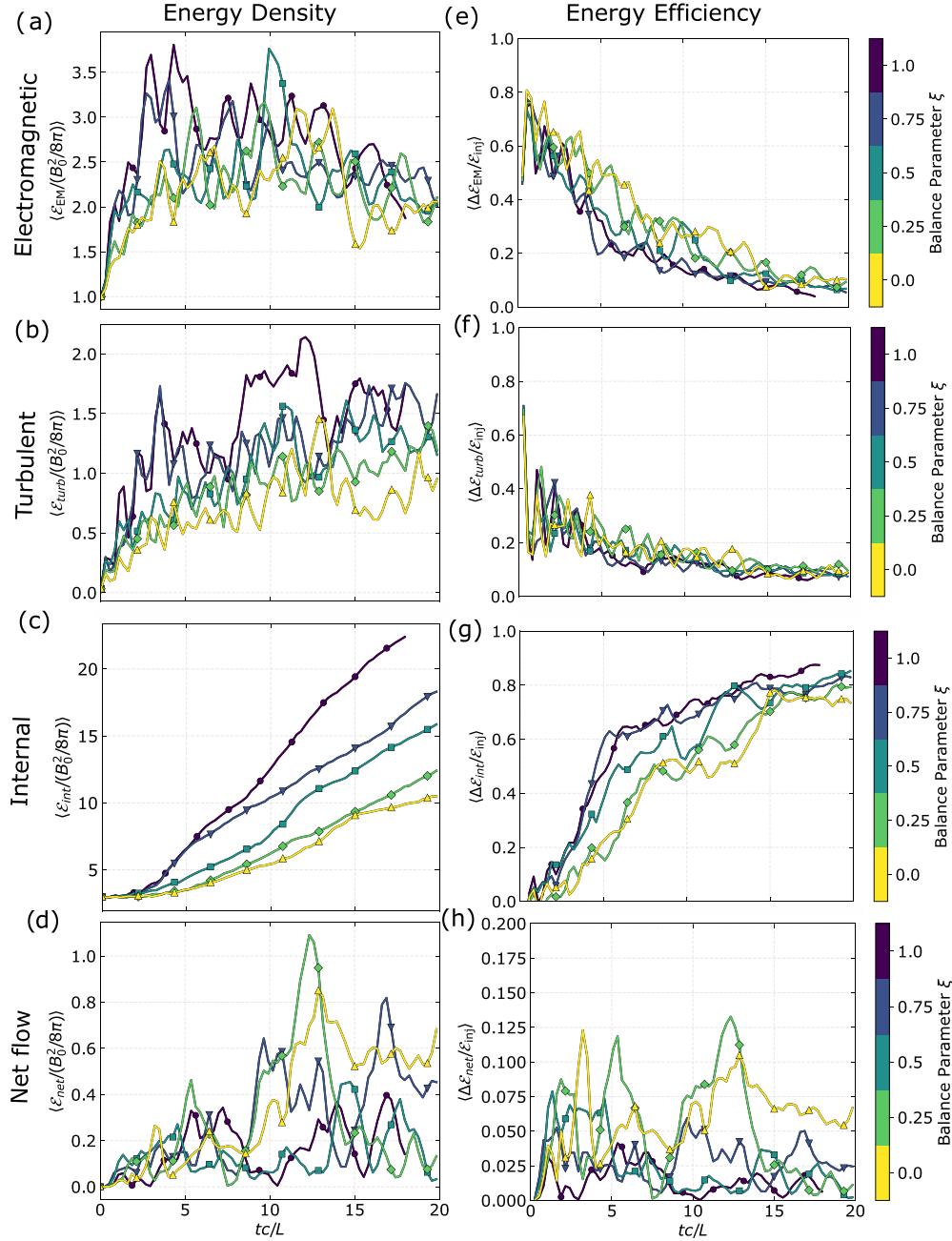
Figure 3. Energy partition into electromagnetic, turbulent kinetic, internal, and net flow energy depends on balance parameter. Left-hand column: each type of energy density evolved over time, normalized to the constant value of the initial magnetic energy density $B_0^2/8\pi$. The turbulent electromagnetic (a) and kinetic (b) energy densities reach a constant value whereas the internal (c) and net flow (d) energy densities increase over time. Right-hand column: the change in each type of energy density evolved over time, normalized to the total amount of injected energy density $\mathcal{E}_{inj}(t)$. Summing over the four panels on the right for each simulation adds to 1. Turbulent electromagnetic (e) and kinetic (f) energy efficiencies decay as $\propto t^{-1}$, whereas internal (g) and net flow (h) energy efficiencies saturate at a constant fraction of the injected energy. Note that the net flow energy (h) has a different vertical axis. Colours and markers indicate balance parameter. These simulations all have $L/2\pi\rho_{e0} = 81.5$.

shown). This decrease in electric energy density could be due to the decrease in the plasma velocity, which is approximately the Alfvén speed: $E \sim (\delta v/c) \times B \sim (v_A/c)B_0$. Faster heating in the balanced turbulence case leads to smaller v_A and hence smaller electric field. The simulations show that the time-averaged turbulent kinetic energy density $\langle \overline{\Delta\mathcal{E}_{turb}} \rangle$ also depends on ξ, increasing from 75 per cent of the background magnetic energy for the most imbalanced case ($\xi = 0.0$) to about 125 per cent for balanced turbulence with $\xi = 1.0$ (Fig. 5b).

The smaller values of $\langle \overline{\Delta\mathcal{E}_{mag}} \rangle$ and $\langle \overline{\Delta\mathcal{E}_{turb}} \rangle$ in the imbalanced case result from the injection of less energy in this case (Fig. 2). The fraction of injected energy that converts into turbulent and magnetic energy (i.e. the corresponding energy efficiencies) at any given time is almost independent of balance parameter (Figs 3e, f), with slightly higher $\langle \Delta\mathcal{E}_{EM} \rangle/\langle \mathcal{E}_{inj} \rangle$ for $\xi = 0$ compared to $\xi = 1$.

To test whether the turbulence is Alfvénic, we use the 'Alfvén ratio' $r_A \equiv \langle \overline{\Delta\mathcal{E}_{turb}} \rangle/\langle \overline{\Delta\mathcal{E}_{mag}} \rangle$. The Alfvén ratio is related to the
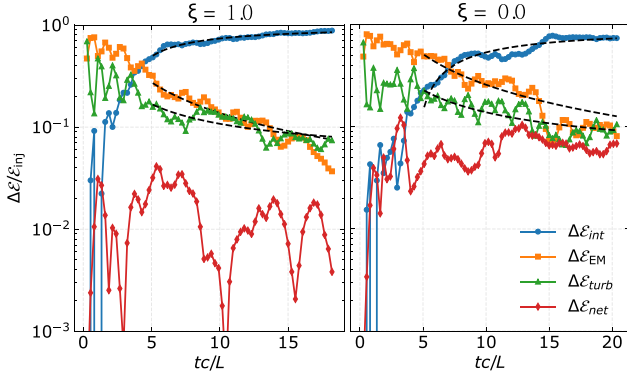
Figure 4. Time evolution of the energy partition for the balanced case ($\xi = 1.0$; left-hand panel) and most imbalanced case ($\xi = 0.0$; right-hand panel). Both show a decay in turbulent electromagnetic and kinetic energies and a saturation of internal and net flow energy densities; black dashed lines show fits to $A + B/t$, with A and B constants. The imbalanced case has net flow energy density about an order of magnitude higher than the balanced case and correspondingly lower internal energy density, whereas the turbulent electromagnetic and kinetic energy densities are comparable for both balance parameters.

residual energy E_r (defined as the difference between the turbulent kinetic and turbulent magnetic energies) via $E_r = (r_A - 1)/(r_A + 1)$. Ideal MHD predicts that the time- and volume-averaged kinetic and perturbed magnetic energies in an Alfvén wave (and thus perfectly imbalanced turbulence) should be in equipartition: $r_A = 1$. We might expect the same Alfvén ratio for turbulence (both balanced and imbalanced) comprising many Alfvén waves – though due to an increase in non-linear interactions, physical plasmas such as the solar wind often have an excess of magnetic energy such that $r_A \approx 0.7$ (Chen et al. 2013; Chen 2016); see Boldyrev & Perez (2009), Boldyrev et al. (2011), and Wang, Boldyrev & Perez (2011) for MHD models of this excess. Our simulations show that both balanced and imbalanced turbulence are in equipartition to within error bars (Table 2). The standard deviations of mean values for $\langle \overline{\Delta \mathcal{E}_{\text{turb}}} \rangle$ and $\langle \overline{\Delta \mathcal{E}_{\text{mag}}} \rangle$ in Table 2 were calculated for the $L/2\pi \rho_{e0} = 81.5$ and $L/2\pi \rho_{e0} = 40.7$ simulations (nine values for each balance parameter) and summed in quadrature. These error bars suggest that the large-scale ratio of turbulent kinetic to magnetic energies is independent of ξ. However, the residual energy may have

Table 2. The turbulence in all simulations of balanced and imbalanced turbulence is approximately Alfvénic. The Alfvén ratio $r_A = \langle \overline{\Delta \mathcal{E}_{\text{turb}}} \rangle / \langle \overline{\Delta \mathcal{E}_{\text{mag}}} \rangle$ is approximately 1 for the largest simulations ($L/2\pi \rho_{e0} = 81.5$) for all values of the balance parameter ξ. Standard deviations are calculated from the statistical seed studies at each balance parameter.

ξ	$\langle \overline{\Delta \mathcal{E}_{\text{turb}}} \rangle / \langle \overline{\Delta \mathcal{E}_{\text{mag}}} \rangle$
1.0	1.1 ± 0.3
0.75	1.2 ± 0.2
0.5	1.0 ± 0.1
0.25	1.0 ± 0.1
0.0	0.9 ± 0.1

a scale-dependent power-law spectrum with significant dependence on imbalance, which we do not address here. The solar wind shows a clear dependence of the residual energy spectrum's slope on imbalance, with a value of -2 for balanced turbulence and closer to -1.8 for totally imbalanced turbulence (Chen et al. 2013). The dependence of the residual energy spectrum's slope on imbalance is a major outstanding puzzle that has not been successfully addressed by any phenomenological model of imbalanced turbulence thus far.

Our finding of approximate equipartition indicates that the turbulence is predominantly Alfvénic. In addition to Alfvén waves, slow and fast compressive modes also contribute to the turbulence. The fast modes, introduced by the OLA driving (Zhdankin 2021) or non-linear relativistic wave conversion (Takamoto & Lazarian 2016), and the slow modes, passively mixed by the turbulence (Lithwick & Goldreich 2001), lead to total density fluctuations on the order of 20–30 per cent of the background density in our simulations (not shown). Though the presence of fast and slow modes could affect the Alfvén ratio, characterizing their contribution is beyond the scope of this study.

3.2.3 Internal energy

The increase in internal energy dominates the plasma energy budget at late times. Though the initial internal energy starts out at about three times the initial magnetic energy for all balance parameters, the plasmas with balanced turbulence heat up almost twice as quickly as the plasmas with imbalanced turbulence (Fig. 3c). At late times, about 80 per cent of the injected energy is converted into internal energy in the imbalanced case ($\xi = 0$), slightly lower than the
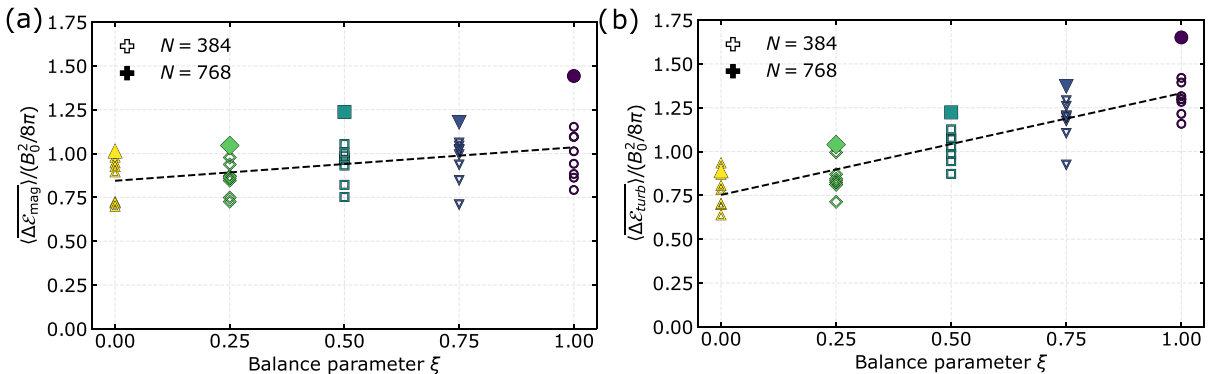

Figure 5. Trends of the turbulent magnetic and kinetic energy densities with balance parameter. Quantities are time-averaged from $10 < tc/L < 20$. The largest domain size $L/2\pi \rho_{e0} = 81.5$ (filled markers) shows a linear trend with balance parameter for the turbulent magnetic (a) and kinetic (b) energy densities, respectively. The statistical deviation is shown by the $L/2\pi \rho_{e0} = 40.7$ seed study (unfilled markers). The dashed lines show linear fits. Colours and markers are the same as in Fig. 3.
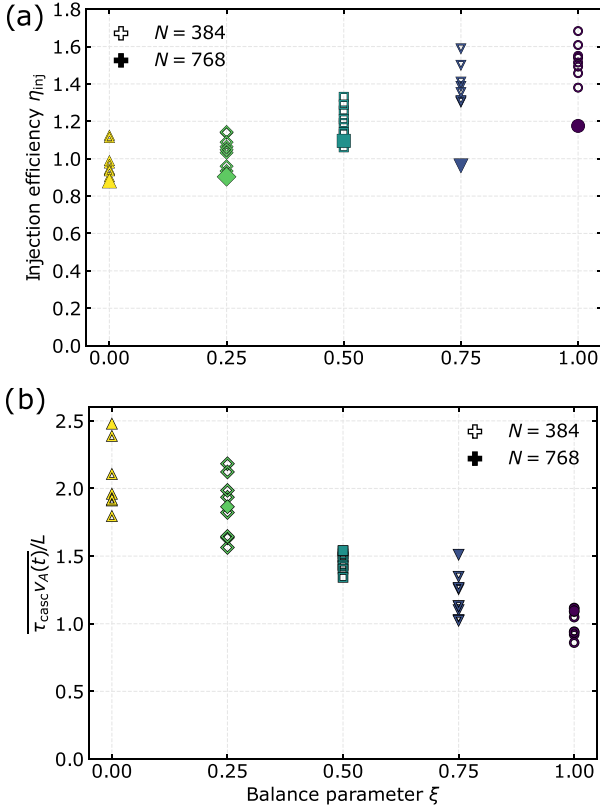
Figure 6. The injection efficiency η_{inj} (a; equation 18) and cascade time τ_{casc} (b; equation 19) depend on balance parameter. The largest domain size $L/2\pi\rho_{e0} = 81.5$ is shown with filled markers and the statistical deviation is shown by the $L/2\pi\rho_{e0} = 40.7$ seed study (unfilled markers). Colours and markers are the same as in Fig. 3.

corresponding value of closer to 90 per cent for the balanced case (Fig. 3g).

Because the plasma's internal energy increases linearly after an initial transient, we characterize its heating rate (i.e. slope) through the dimensionless 'injection efficiency' parameter η_{inj}. We define this order-unity coefficient as the ratio of the plasma heating rate $\langle\dot{\mathcal{E}}_{\text{int}}\rangle(t)$ to a 'reference' heating rate $\langle\dot{\mathcal{E}}_{\text{ref}}\rangle$. We define $\langle\dot{\mathcal{E}}_{\text{ref}}\rangle$ by dividing the turbulent magnetic energy density, $\delta B_{\text{rms}}^2/8\pi$, by a characteristic non-linear cascade time at the outer scale $L/\delta v_{\text{rms}} \sim L/(v_{A0}\delta B_{\text{rms}}/B_0)$, assuming strong Alfvénic turbulence and $v_{A0}/c \ll 1$. This formulation gives us an operational definition of the injection efficiency in terms of quantities that can be directly measured in our simulations at any moment of time:

$$\eta_{\text{inj}} \equiv \frac{\langle\dot{\mathcal{E}}_{\text{int}}\rangle}{\langle\dot{\mathcal{E}}_{\text{ref}}\rangle} = \frac{8\pi B_0 L \langle\dot{\mathcal{E}}_{\text{int}}\rangle}{\delta B_{\text{rms}}^3 v_{A0}}. \qquad (18)$$

The injection efficiency quantifies how efficiently turbulent magnetic energy cascades to small scales and dissipates. The heating rate of the plasma is extracted by fitting the slope of the internal energy in the interval $5 < tc/L < 20$ and converting to the injection efficiency via equation (18), taking the value of δB_{rms} as the time-average over the same time period. The statistical mean value of the injection efficiency varies from about 1.0 for the most imbalanced case ($\xi = 0.0$) to about 1.5 for the balanced case ($\xi = 1.0$) as seen in Fig. 6(a), with a statistical standard deviation on the order of 0.2.

As discussed in Section 3.2.2, the magnitude of the magnetic field fluctuations depends on balance parameter, which in principle

may influence energy dissipation and the injection efficiency. To verify that the trend in the injection efficiency η_{inj} with balance parameter ξ is not due to the variation of the amplitude of magnetic energy perturbations $\delta B_{\text{rms}}^2/B_0^2$ with ξ, we ran a simulation of imbalanced turbulence with $\xi = 0$ and a driving amplitude $\sqrt{2}$ times its canonical value. The magnetic field fluctuation level δB_{rms}^2 changes from $0.8B_0^2$ for the unadjusted amplitude case to $1.2B_0^2$ for the increased amplitude case, consistent with the unadjusted amplitude of the balanced case with the same random seed. The injection efficiency, however, increases to 1.1 with the increased amplitude, compared to 0.9 for the unadjusted $\xi = 0$ case and 1.4 for the unadjusted $\xi = 1$ case with the same random seed. Thus, two simulations with the same level of magnetic field perturbations but different balance parameters experience significantly different injection efficiencies, suggesting that the injection efficiency has an inherent dependence on balance parameter rather than δB_{rms}. This result suggests that the cascade time depends on balance parameter.

To explore the possibility that the cascade time τ_{casc} depends on balance parameter, we define

$$\tau_{\text{casc}} \equiv \frac{\langle\Delta\mathcal{E}_{\text{EM}} + \mathcal{E}_{\text{turb}}\rangle}{\langle\dot{\mathcal{E}}_{\text{int}}\rangle}. \qquad (19)$$

The cascade time is normalized to the global Alfvén time $L/v_A(t)$ and then time-averaged over $10 < tc/L < 20$ (i.e. $5.8 < tv_{A0}/L < 11.6$). We expect the cascade time to be on the order of an Alfvén time for an Alfvénic cascade, and for balanced turbulence we indeed find that the cascade time varies statistically between 0.8 and 1.2 $L/v_A(t)$ (Fig. 6b). However, the cascade time increases to about 2.2 $L/v_A(t)$ on average for the imbalanced case $\xi = 0$. The lack of overlap between the cascade times of imbalanced and balanced turbulence suggest that the difference is statistically significant, rather than a fluke of random seeds. A longer cascade time for more imbalanced turbulence is consistent with Lithwick et al. (2007)'s suggestion that the dominant waves are less strongly scattered in the imbalanced case.

3.3 Net flow energy and momentum transfer

As a component of the energy not present in balanced turbulence, we expect the kinetic energy in the net motion of the plasma through the simulation domain to depend on the balance parameter. In the balanced case, the statistically symmetric (although not necessarily momentum conserving) driving should on average lead to no net motion. In contrast, because imbalanced driving breaks the symmetry along the background magnetic field, we may expect a non-zero net flow energy for $\xi < 1.0$ if the asymmetric wave momentum converts into plasma momentum. In a gravitational potential, the net flow that results from efficient wave-plasma momentum coupling could form a wind or outflow. In this section, we first propose a simple model for the properties of such a net flow (Section 3.3.1) and then compare to numerical results (Section 3.3.2).

3.3.1 Analytic framework for momentum transfer

A net flow could result from the efficient transfer of injected wave momentum into plasma momentum. In this section, we propose that the net flow velocity should be constant and provide a scaling for its magnitude. We can write the net flow energy density as

$$\mathcal{E}_{\text{net}}(t) = (\Gamma_{\text{net}}(t) - 1)\langle\rho\rangle(t)c^2 \approx \frac{\langle\dot{\mathcal{E}}_{\text{int}}\rangle(t)v_{\text{net}}^2(t)}{2c^2}, \qquad (20)$$

where the last expression holds for $v_{\text{net}}(t) \ll c$. We have defined the net Lorentz factor $\Gamma_{\text{net}}(t) = (1 - v_{\text{net}}^2/c^2)^{-1/2}$.

Analogously, the internal energy density relates to the net plasma momentum density as

$$\langle \mathcal{P}_{z,\text{tot}} \rangle(t) = \Gamma_{\text{net}}(t) \langle \rho \rangle(t) v_{\text{net}}(t) \approx \frac{\langle \mathcal{E}_{\text{int}} \rangle(t)}{c^2} v_{\text{net}}(t), \tag{21}$$

where again $v_{\text{net}} \ll c$ in the last expression. In simulations, both $\mathcal{E}_{\text{net}}(t)$ and $\langle \mathcal{P}_{z,\text{tot}} \rangle(t)$ increase linearly in time (Section 3.3.2). Because these two quantities depend on different powers of v_{net}, we deduce that the net velocity should be relatively constant in time. We test this prediction in the next section.

We can understand the net flow as a relativistic effect. As a limiting case, assume that the maximal asymmetric Poynting flux for a single Alfvén wave $|\langle S_z \rangle_{1-\text{wave}}|$ (equation 10) is injected into a plasma. If a fraction ϵ of the momentum density $|\langle S_z \rangle_{1-\text{wave}}|/c^2$ in this electromagnetic wave converts into the plasma momentum density $\langle \mathcal{P}_{z,\text{tot}} \rangle$, we have

$$\langle \mathcal{P}_{z,\text{tot}} \rangle = \epsilon \frac{\langle \delta B^2 \rangle v_{A0}}{4\pi c^2} = \Gamma_{\text{net}} \langle \rho \rangle v_{\text{net}}, \tag{22}$$

where the last equality follows from equation (21). By writing the relativistic mass density $\langle \rho \rangle = \langle \gamma \rangle m_e n_0$, we find

$$\Gamma_{\text{net}} v_{\text{net}} = \frac{\langle \delta B^2 \rangle}{4\pi \langle \rho \rangle c^2} \epsilon v_{A0} = \frac{4}{3} \epsilon \, \delta\sigma \, v_{A0} \tag{23}$$

$$v_{\text{net}} = c\epsilon \sqrt{\frac{16 \, \delta\sigma^2 \, v_{A0}^2/c^2}{9 + 16 \, \delta\sigma^2 \, v_{A0}^2/c^2}} \rightarrow \frac{4}{3} \epsilon \, \delta\sigma \, v_{A0}, \tag{24}$$

where we have defined $\delta\sigma = \langle \delta B^2 \rangle/(4\pi h)$ and the last expression again holds for $v_{\text{net}} \ll c$. From equation (24), we see that the net flow's velocity approaches 0 as the magnetization goes to 0. Though the efficiency ϵ of converting electromagnetic momentum into plasma momentum can never be greater than 1, it could change with σ.

3.3.2 Numerical results for momentum transfer

In this section, we test the assumptions behind the above calculations and demonstrate that our simulations do indeed find a net flow in line with the above framework.

Our simulations find that about 8 per cent of the injected energy converts into net flow energy even in the most imbalanced case ($\xi = 0.0$), a fraction that becomes comparable to the turbulent electromagnetic or kinetic energy efficiencies after the latter two have decayed by a factor of two or more, around 15 L/c (Fig. 4). Since the net flow efficiency fluctuates strongly about a mean value in time, we compare different balance parameters by averaging over $10 < tc/L < 20$. The result, shown in Fig. 7, reveals that the net flow efficiency increases with decreasing ξ, as expected. The mean over an ensemble of identical simulations with $\xi = 0$ and varying random seeds is about 0.06, approximately three times as large as that for the balanced turbulence (about 0.02). The statistical spread in the balanced case is on the order of 0.01, and about 0.03 for the imbalanced case. Because energy is a strictly positive quantity and a limited number of modes were driven, even the simulations of balanced turbulence ($\xi = 1.0$) have a non-zero (albeit small) net flow energy due to short periods of net motion. Notably, there are three prominent outliers in Fig. 7 in the magnitude of the net flow efficiency in simulations with balance parameters $\xi = 0.5, 0.75,$ and 1.0. Each of these outlying simulations was initialized with the same random seed, suggesting that the particular random phases of the driven modes resulted in non-zero mean velocity later in the simulations' evolutions. The presence of these outliers demonstrates the need for a suite of random seeds to tease out statistically robust trends.
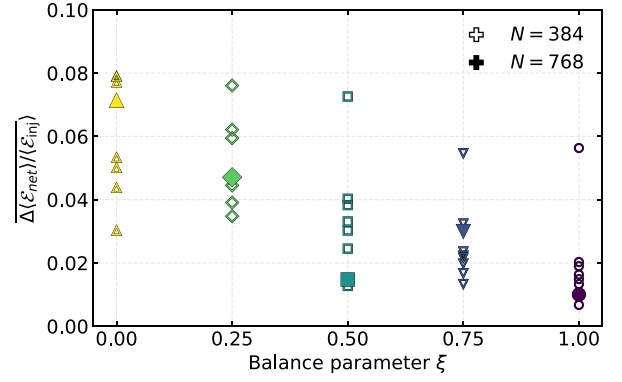

Figure 7. The net flow energy efficiency decreases with increasing balance parameter. The plotted values are volume-averaged and time-averaged from $10 < tc/L < 20$. The largest domain size $L/2\pi \rho_{e0} = 81.5$ is shown with filled markers and the statistical deviation is shown by the $L/2\pi \rho_{e0} = 40.7$ seed study (unfilled markers). Note that the outliers for $\xi = 0.5, 0.75,$ and 1.0 with net flow energy efficiencies a factor of 2 higher than the rest of the seed study were run with the same random seed. Colours and markers are the same as in Fig. 3.

Although the net flow energy density demonstrates the importance of the net flow in the overall energy budget, it does not contain information about the direction of the plasma's net motion. To address this issue, we now examine momentum rather than energy. First, we discuss the injected electromagnetic momentum and look at the Poynting flux $S = (c/4\pi)E \times B$. For balance parameters $\xi < 1.0$, we expect the driven waves' Poynting flux to be non-zero along the background magnetic field ('parallel Poynting flux'; S_z). The spatial distribution of the parallel Poynting flux, plotted in Fig. 8, is highly non-uniform. Similar to MHD turbulence (Perez & Boldyrev 2009), our balanced simulation has local patches of strong Poynting flux and thus high imbalance, highlighting the fundamental connection between balanced and imbalanced turbulence at small scales. The total, volume-averaged parallel Poynting flux $\langle S_z \rangle$ is statistically constant in time and, for the balanced case ($\xi = 1.0$), oscillates around zero (Fig. 9a). After time-averaging over the period from $10 < tc/L < 20$, the parallel Poynting flux is clearly positive for imbalanced turbulence and consistent with zero for balanced turbulence (Fig. 9b). The value $\overline{\langle S_z \rangle} \approx 0.2 \, (cB_0^2/4\pi)$ at $\xi = 0.0$ is about 30 per cent of the limiting value $(\delta B/B_0)^2 v_A/c \, (cB_0^2/4\pi) \approx v_A/c \, (cB_0^2/4\pi) \approx 0.58 \, (cB_0^2/4\pi)$ expected for a single Alfvén wave (equation 10). The decrease in the Poynting flux with increasing balance parameter agrees well with the quadratic fit predicted by equation (11), as shown by the dotted and dash-dot black lines in Fig. 9(b), though we do not rule out a linear dependence. The same outliers discussed for the net flow efficiency are present in the parallel Poynting flux. The time- and volume-averaged Poynting flux in the x- and y-directions are much smaller than the parallel Poynting flux: within 0.1 $(c \, B_0^2/4\pi)$ of zero for all balance parameters (not shown), indicating that the net electromagnetic momentum is primarily along the background magnetic field.

The injected Poynting flux imparts net momentum to the plasma. In agreement with the interpretation in Section 3.2.1, the volume-averaged parallel momentum $\langle \mathcal{P}_{z,\text{tot}} \rangle$ of the plasma increases approximately linearly over time (Fig. 9c). The ratio $\langle \mathcal{P}_{z,\text{tot}} c^2 \rangle / (\langle S_z \rangle t v_{A0}/L)$, shown in Fig. 9(d), is approximately constant in time and fluctuates around values of the order of unity for any given balance parameter. In this figure, the parallel Poynting flux has been converted to an electromagnetic momentum density $\langle S_z \rangle/c^2$,
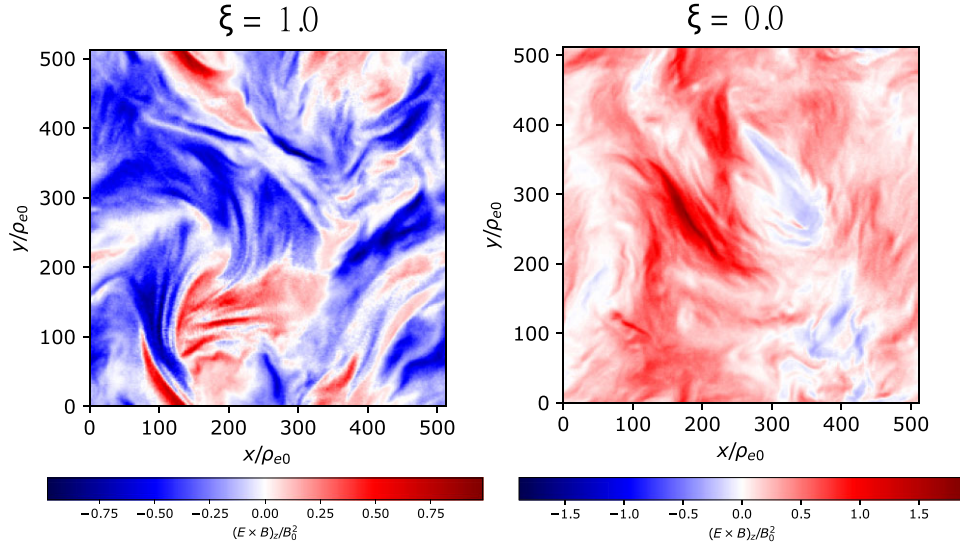
Figure 8. Even turbulence that is balanced as a whole has spatial and temporal pockets of locally imbalanced turbulence. Slices of the Poynting flux $(c/4\pi)\boldsymbol{E} \times \boldsymbol{B}$ in the z-direction, taken at the plane $z = 0$ at time $t = 16.1\ L/c$ and normalized to $(c/4\pi)B_0^2$ for balanced turbulence ($\xi = 1.0$; left-hand panel) and most imbalanced turbulence ($\xi = 0.0$; right-hand panel) show variation in the sign of Poynting flux throughout the domain.
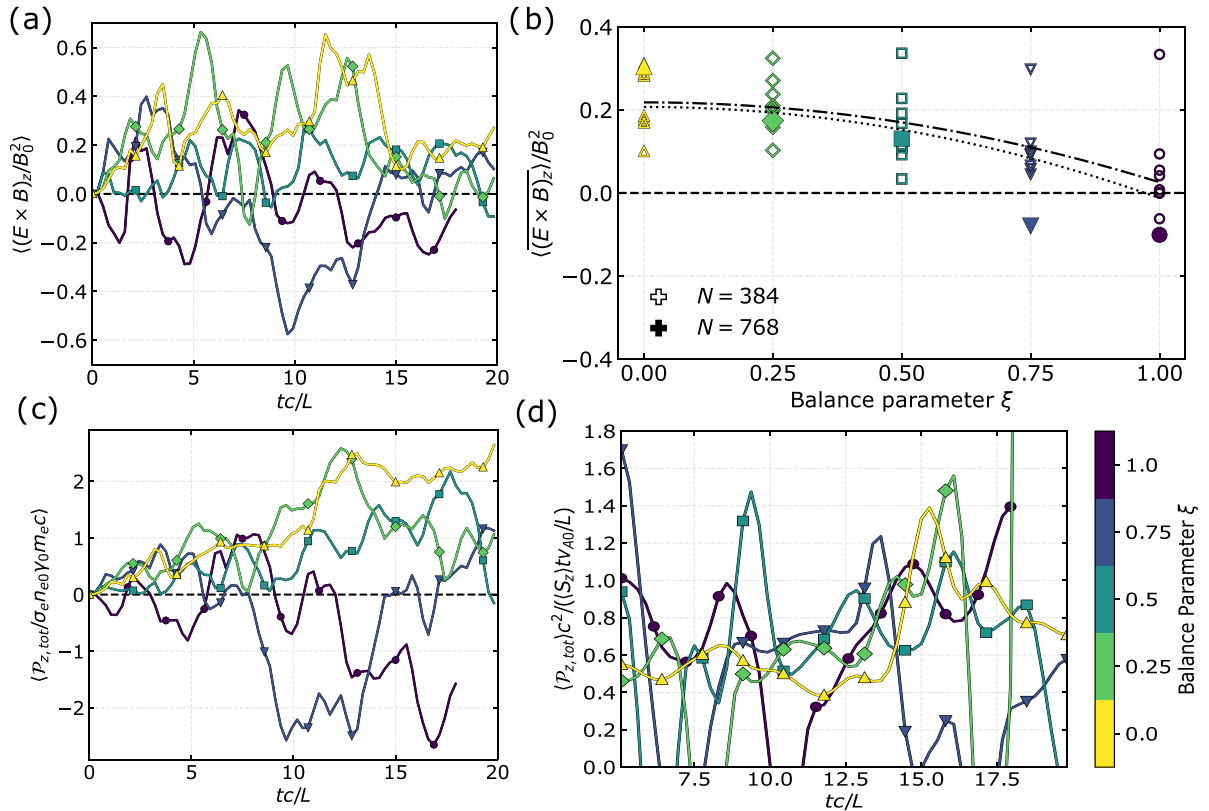

Figure 9. The average parallel Poynting flux is approximately constant in time, whereas the z-momentum of the plasma increases linearly in time. (a) The time evolution of the volume-averaged Poynting flux $(c/4\pi)\langle\boldsymbol{E} \times \boldsymbol{B}\rangle$ in the z-direction, normalized to $(c/4\pi)B_0^2$, shows fluctuations around some mean value; time-averaging the curves over $10 < tc/L < 20$ shows a quadratic dependence on balance parameter (b). The time evolution (c) of the parallel plasma momentum shows an increase in time. The ratio $\langle\mathcal{P}_{z,\text{tot}}c^2\rangle / (\langle S_z\rangle\ tv_{A0}/L)$, shown in (d), is of the order of unity for all values of balance parameter. The black dash-dot lines show a quadratic fit; the dotted line is a quadratic fit without the outlier seed. The dashed black lines indicate zero. Colours and markers are the same as in Fig. 3.

and the momentum densities of both the plasma and the electromagnetic waves are normalized to $g_0 \equiv B_0^2/(4\pi c)$, allowing for direct comparison between the two quantities. The ratio of the volume averages has been smoothed with a Hanning window to remove arbi-

trarily large values due to a small Poynting flux. To further illustrate the relationship between $\langle S_z\rangle$ and $\langle\mathcal{P}_{z,\text{tot}}\rangle$, Fig. 10 shows their values at each time snapshot (given by individual dots) for each balance parameter (shown via marker and colour). In general, the plasma
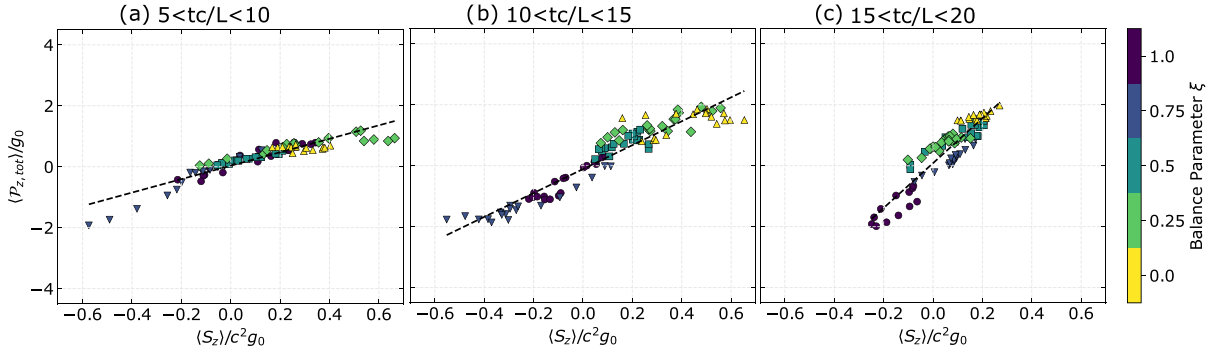
Figure 10. The parallel electromagnetic momentum generates and maintains the parallel momentum of the plasma. In these plots, each point corresponds to the instantaneous values of the volume-averaged plasma momentum along the background magnetic field and the volume-averaged parallel electromagnetic momentum at a given simulation time. Three periods of time are shown with linear fits of slopes 2.2, 3.9, and 7.4 for (a) $5 < tc/L < 10$, (b) $10 < tc/L < 15$, and (c) $15 < tc/L < 20$, respectively. Here, $g_0 = B_0^2/(4\pi c)$ is a typical value of momentum density. Colours and markers are the same as in Fig. 3.
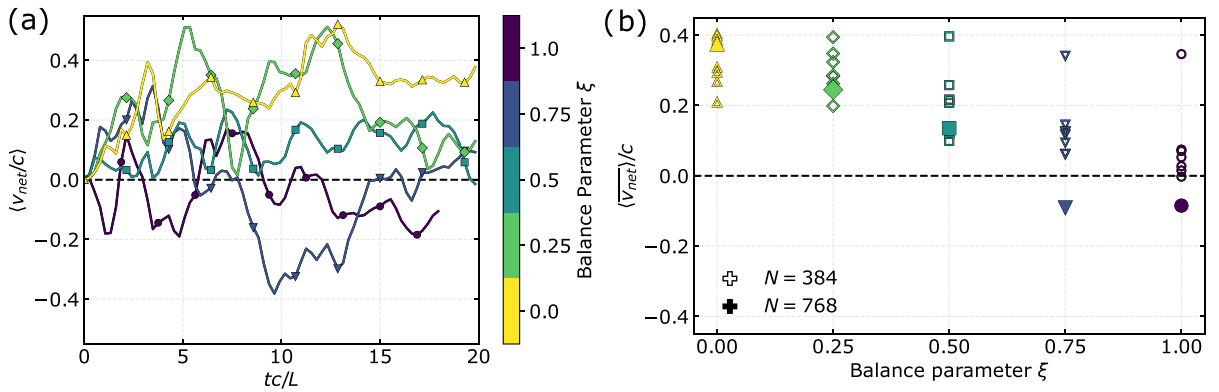
Figure 11. The net plasma velocity along the background magnetic field depends on balance parameter. (a) The time evolution of the volume-averaged velocity v_{net} (equation 21) shows values that fluctuate in time around some mean value that depends on ξ; time-averaging the curves over $10 < tc/L < 20$ shows a dependence on balance parameter (b). The largest domain size $L/2\pi\rho_{e0} = 81.5$ is shown with filled markers and the statistical deviation is shown by the $L/2\pi\rho_{e0} = 40.7$ seed study (unfilled markers). Colours and markers are the same as in Fig. 3. The black dashed lines show zero.

momentum dominates over the electromagnetic momentum, with a time-dependent ratio given by the slope of the linear fit. The positive ratio shows that a positive volume-averaged parallel electromagnetic momentum corresponds to a positive parallel plasma momentum, as expected if Poynting flux converts to plasma momentum. The balanced turbulence's electromagnetic momentum and plasma momentum span both positive and negative values; for more imbalanced turbulence, the distribution shifts up and right, demonstrating that the asymmetric driving of electromagnetic momentum results in asymmetric net motion of the plasma in the *z*-direction.

Using equation (21) to solve for v_{net} shows that v_{net} fluctuates around a mean value dependent on balance parameter (Fig. 11a). The net velocity of the plasma with balanced turbulence oscillates around zero, never reaching more than $0.2c$. The plasmas with the most imbalanced turbulence can reach net velocities up to $0.5c$. Averaging over $10 < tc/L < 20$ shows a clear dependence of the net velocity on balance parameter (Fig. 11b). As expected, plasmas with balanced turbulence experience a time-averaged net velocity near zero, though the finite simulation duration means that temporary movements parallel or antiparallel to the background magnetic field are not completely averaged out. Equation (24) predicts a net velocity of $0.4c$ for the most imbalanced turbulence (plugging in four waves with $\delta B \sim B_0$, and setting $\sigma_0 = 0.5$, $v_{A0} = 0.58c$, and $\epsilon = 1$), remarkably close to the values found in Fig. 11(b).

Previous studies of imbalanced turbulence appear to exclude the possibility of generating net plasma motion along the background magnetic field, either through the assumption of reduced MHD, gyrokinetics, or force-free description (Perez et al. 2012; Cho & Lazarian 2014; Meyrand et al. 2021). As such, this work presents, to our knowledge, the first numerical demonstration and investigation of net flow due to imbalanced turbulence. Such a large net motion of the plasma may have implications for driving accretion disc winds, particularly if the wind comprises mostly non-thermal particles.

3.4 Non-thermal particle acceleration

Non-thermal particle acceleration can explain high-energy flares and power laws seen in spectra of various astrophysical systems. Studying NTPA self-consistently requires PIC simulations. Recent PIC simulations of turbulence (Zhdankin et al. 2017, 2018a; Comisso & Sironi 2018, 2019) have successfully produced non-thermal particle populations that result in power-law spectra. Similar results have been produced in PIC simulations of kink-unstable jets (Alves, Zrake & Fiuza 2018; Davelaar et al. 2020) and the magnetorotational instability in accretion discs (Riquelme et al. 2012; Hoshino 2013; Kunz, Stone & Quataert 2016), where turbulence may play a fundamental role in the particle acceleration. Because power-law spectra
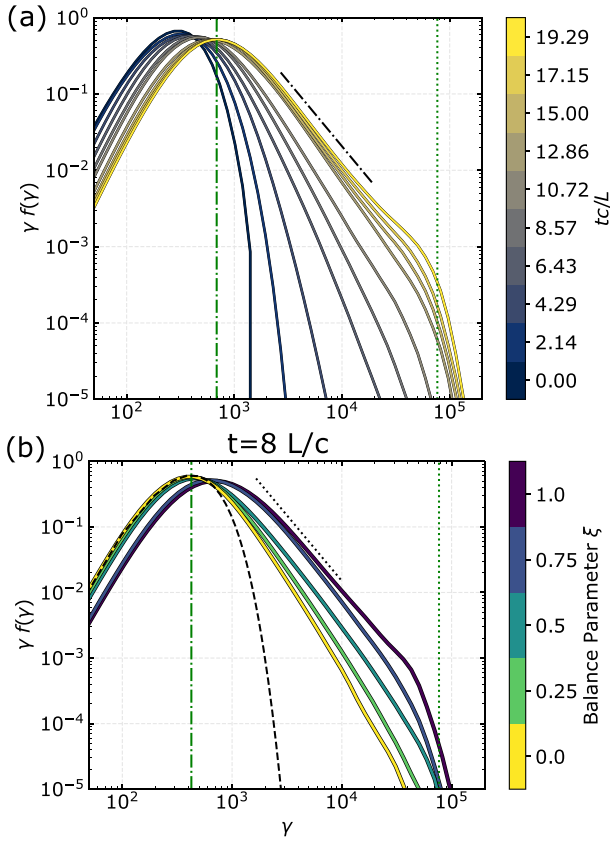
Figure 12. Particle acceleration occurs for all values of balance parameter. (a) The distribution function of the most imbalanced case ($\xi = 0.0$) becomes shallower in time from an initial Maxwell–Jüttner distribution (purple) to a Maxwell–Jüttner distribution plus a hard power-law component at later times (yellow). (b) Spectra taken at the same time $t = 8.0$ L/c for different balance parameters show different peak energies but similar power-law components. The dashed black line shows a Maxwell–Jüttner fit to the $\xi = 0.0$ case. The vertical green dash-dot line shows the mean Lorentz factor $\langle\gamma\rangle$ extracted from this fit. The vertical green dotted line shows the maximum energy $\gamma_{\max}$. The dash-dot black line in panel (a) shows the power-law $\gamma^{-2.7}$, while the dotted black line in panel (b) shows γ^{-3}. Colours are the same as in Fig. 3.

are observed in systems with asymmetric energy injection, it is important to understand how imbalance affects particle acceleration.

We find that imbalanced turbulence can accelerate a significant portion of the plasma's particles to suprathermal energies (Fig. 12), much like balanced turbulence at similar magnetizations $\sigma \sim 1$. Even the most imbalanced case $\xi = 0.0$ shows the development of a high-energy power-law tail, which hardens and reaches an asymptotic slope after about 12 L/c (Fig. 12a). At late times $t \gtrsim 12$ L/c, the simulation domain's boundary conditions limit the maximum attainable Lorentz factor to $\gamma_{\max} = LeB_0/m_ec^2$, resulting in the 'pile-up' of high-energy particles at $\gamma_{\max}$, followed by a sharp cutoff rather than the continuation of the power law to even higher energies (Zhdankin et al. 2018b). Visually, the non-thermal distribution matches the power-law scaling $f(\gamma) \propto \gamma^{-2.7}$ between $\langle\gamma\rangle$ and $\gamma_{\max}$, shown by the dash-dot line in Fig. 12(a). Comparing turbulence with different balance parameters, we see that more balanced turbulence heats the plasma more quickly and forms a power-law spectrum faster than imbalanced turbulence (Fig. 12b). For particle spectra taken at $t = 8.0$ L/c, the simulation of balanced turbulence $\xi = 1.0$ has already heated to a peak Lorentz factor of about 700 and is experiencing

Table 3. Table of 'equivalent' times t_{eq} in L/c where the same amount of energy density 10.3 $B_0^2/8\pi$ has been injected. Values of the non-thermal particle and energy fraction at t_{eq}, shown in the second and third rows, are discussed in Section 3.4. Equivalent times are labelled in Fig. 2 as red ×'s.

ξ	0.0	0.25	0.5	0.75	1.0
t_{eq}	20.0	17.4	13.1	9.4	8.0
$N_{\text{non-thermal}}/N_{\text{total}}$	0.20	0.19	0.20	0.21	0.21
$\langle\mathcal{E}_{\text{nonthermal}}\rangle/\langle\mathcal{E}_{\text{pl}}\rangle$	0.54	0.53	0.55	0.54	0.54

pile-up, as shown by the spectrum's break around $\gamma \sim 5 \times 10^4$. In contrast, the most imbalanced case $\xi = 0.0$ still has a peak Lorentz factor of around 400 and its power-law index has not yet reached an asymptotic value (Fig. 12b).

Because of the different rates at which energy is injected into simulations with different balance parameters, it may be more meaningful to compare particle spectra not at the same fixed absolute time, but rather at 'equivalent times' when a fixed amount of energy has been injected. For definiteness, we take this time to coincide with the end ($t = 20$ L/c) of the simulation for the most imbalanced case, $\xi = 0$, corresponding to an injected energy of 10.3 $B_0^2/8\pi$. The equivalent times for the simulations vary from 8 L/c for the balanced case $\xi = 1.0$ to 20 L/c for the most imbalanced case $\xi = 0.0$ (Table 3). When compared at these equivalent times, particle spectra for different ξ essentially collapse to a single universal curve (Fig. 13a). In particular, the peak Lorentz factors and the power-law tails up to $\gamma \approx 10^4$ become nearly indistinguishable. This similarity suggests that NTPA operates similarly in balanced and imbalanced turbulence when considered on appropriate time-scales. In particular, the non-thermal segments of the distribution function match the power-law scaling $f(\gamma) \propto \gamma^{-3}$ (dotted line) for all values of balance parameter, suggesting that imbalanced and balanced turbulence accelerate particles with the same asymptotic spectra. Finer differences appear at higher energies when the spectra are compensated by γ^3; whereas the balanced cases $\xi = 1.0$ and 0.75 closely follow this γ^{-3} scaling in the interval $200 \lesssim \gamma \lesssim 4 \times 10^4$, the more imbalanced cases are never quite flat and appear to more closely follow the scaling $\gamma^{-2.7}$ (dash-dot line), as shown in Fig. 13(b). This power-law index of -2.7 matches the power-law index of balanced turbulence particle spectra in smaller box sizes (Zhdankin et al. 2018b), suggesting that pile-up contaminates the spectra. Because the equivalent times for the simulations of imbalanced turbulence are much longer, the high-energy pile-up could be due to a small subpopulation of particles whose stochastic scattering events pushed them to higher energies. Larger simulation domains are needed to determine what influence the high-energy particle pile-up could have on the particle spectra at lower energies.

The partition of the plasma particles' energy $\langle\mathcal{E}_{\text{pl}}\rangle(t)$ into thermal and non-thermal components further demonstrates that non-thermal particles are energetically important in the system. The fraction of non-thermal particles is calculated by subtracting the Maxwell–Jüttner distribution that best fits the total, box-averaged particle distribution up to the peak Lorentz factor from the total distribution function. This fraction reaches 20 per cent of the total number of particles at 20 L/c for the $\xi = 0$ case (Fig. 14a). The balanced case's fraction of non-thermal particles is larger, reaching 25 per cent of the total number of particles by the same time. At 20 L/c, the energy in these particles comprises 55 per cent of the total plasma energy in the imbalanced case, as compared to 65 per cent for the balanced case (Fig. 14b). At equivalent times, the non-thermal fractions of particles and energy do not vary more than
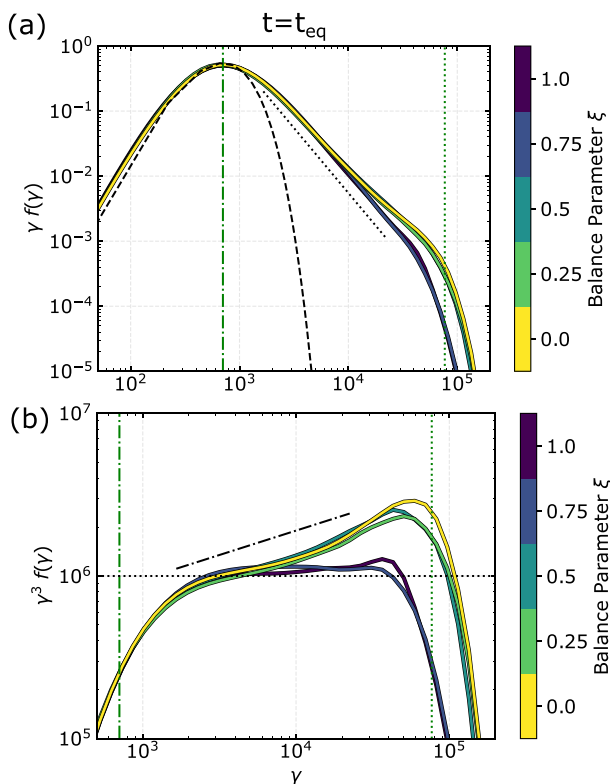
Figure 13. At equivalent times, the power laws of imbalanced turbulence are slightly flatter/harder than balanced turbulence. (a) The particle energy spectra at equivalent times (see Table 3) show a similar mean energy and similar power laws until $\gamma \sim 10^4$. The dashed black line shows a Maxwell–Jüttner fit to the $\xi = 0.0$ case. (b) Compensating by γ^3 reveals that more imbalanced turbulence ($\xi = 0.0, 0.25$, and 0.5) has flatter power laws than the more balanced turbulence with $\xi = 0.75$ or 1.0. The vertical green dash-dot line shows the mean Lorentz factor $\langle \gamma \rangle$ extracted from the Maxwell–Jüttner fit. The vertical green dotted line shows the maximum energy γ_{max}. The black dash-dot line in panel (b) shows the spectrum compensated to γ^3, while the dotted black line shows the power-law γ^{-3+3} (a constant). Colours are the same as in Fig. 3.
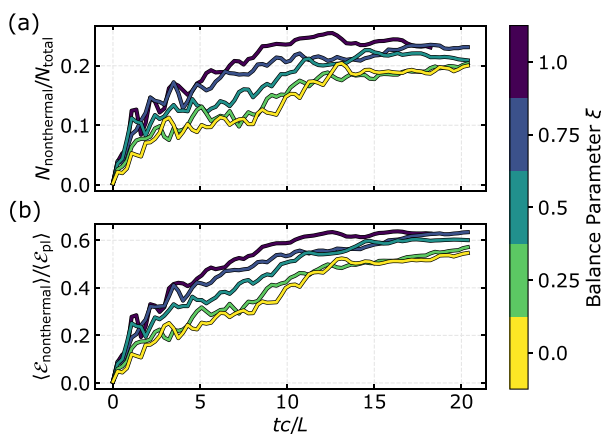

Figure 14. The partition of plasma energy $\langle \mathcal{E}_{\mathrm{pl}} \rangle$ into thermal and non-thermal components shows a moderate increase with the balance parameter at any given time. Both the fraction of particles with non-thermal energies (a) and the fraction of total plasma energy density $\langle \mathcal{E}_{\mathrm{pl}} \rangle$ contained in such particles (b) are calculated by fitting a thermal Maxwell–Jüttner function to the low- and medium-energy particle distribution at each time and subtracting the fit from the total particle distribution. Colours are the same as in Fig. 3.

2 per cent across balance parameters (Table 3), suggesting that particle acceleration by imbalanced turbulence is just as efficient as acceleration by balanced turbulence. For comparison, the fractions for the balanced simulations are slightly smaller than those found for similar simulations of electron–ion plasmas in the relativistically hot limit (Zhdankin et al. 2019).

Though highly idealized, quasi-linear theory can explain many aspects of turbulent NTPA. In particular, the treatment of NTPA as a diffusion in momentum space (Schlickeiser 1989; Chandran 2000) has been justified by measurements of the momentum diffusion coefficient in PIC simulations of balanced turbulence (Comisso & Sironi 2019; Wong et al. 2020) and improved by considering resonance broadening (Demidem, Lemoine & Casse 2020). The original models suggest that the diffusion coefficient scales as $1 - \tilde{H}_c^2$, which is supported by test particle simulations of imbalanced MHD turbulence when parallel acceleration is negligible (Teaca et al. 2014). Our simulations show that imbalance increases the acceleration timescale for NTPA, which is broadly consistent with a decrease in the diffusion coefficient. It is not clear why this increased acceleration time-scale does not affect the power-law index.

4 CONCLUSIONS

In this study we investigate, for the first time, imbalanced kinetic turbulence in a collision-less, magnetized, relativistically hot plasma. Using 3D PIC simulations, we simulate a pair plasma driven by large-scale external currents, creating Alfvén waves propagating parallel and antiparallel to the background magnetic field with different amplitudes. We demonstrate the formation of a turbulent cascade with a similar power-law index for all values of the balance parameter covered by the simulations (Section 3.1). We find that the energy injected into the plasma by the external driving is not only converted into internal energy through small-scale dissipative processes (Section 3.2), but also drives net bulk motion of the plasma (Section 3.3). This efficient transfer of momentum to the plasma appears as a relativistic effect, resulting in a net plasma velocity $\Gamma_{\mathrm{net}} v_{\mathrm{net}} \sim \delta\sigma \, v_{A0}$. We also find efficient particle acceleration over two decades of particle Lorentz factor even for our most imbalanced turbulence (Section 3.4).

Our results on imbalanced turbulence should apply to high-energy astrophysical systems with asymmetric energy injection, such as accretion disc coronae, relativistic jets, and pulsar wind nebulae. We find that NTPA remains efficient in imbalanced turbulence, meaning that particle acceleration models developed for balanced turbulence are still applicable to astrophysical systems with asymmetric energy injection. In addition, our finding that the momentum from the driven Alfvén waves efficiently transfers to the plasma itself constitutes a new mechanism for propelling winds from, for instance, the surface of a turbulent accretion disc. This efficient momentum transfer could also amplify existing astrophysical outflows.

This work represents an important step in studying global properties of imbalanced turbulence in collision-less plasmas. It demonstrates a method for driving imbalanced turbulence in PIC simulations and develops diagnostics to study the unique aspects of imbalanced turbulence, including net motion of the plasma. Our study has revealed a number of factors that could influence the development of imbalanced turbulence and should be further explored: the driving mechanism, the amplitude of magnetic field fluctuations, and the plasma magnetization, to name a few. Our main findings of efficient NTPA and efficient momentum transfer merit further investigation: how are the Fokker–Planck momentum diffusion and advection coefficients for NTPA modified by imbal-

ance? How does the momentum transfer manifest in a more realistic system with density gradients? Thus far, our finding of a net flow is a momentum-transfer mechanism, not a wind-launching mechanism. More work is needed to determine how the transfer efficiency changes with σ and whether the wind comprises the thermal bulk of particles or non-thermal particles. Simulations of imbalanced turbulence in non-relativistic, semirelativistic, and transrelativistic electron–ion plasmas, particularly relevant to accretion flows, will also be important for understanding the fraction of energy that heats electrons. Understanding these aspects of imbalanced turbulence will aid in modelling astrophysical systems with asymmetric energy injection, such as accretion disc coronae, relativistic jets, and pulsar wind nebulae.

DATA AVAILABILITY

The simulation data underlying this article were generated at the XSEDE/TACC Stampede2 supercomputer and are archived at the TACC/Ranch storage facility. As long as the data remain in the archive, they will be shared on reasonable request to the corresponding author.

REFERENCES

Abdo A. A. et al., 2009, Phys. Rev. Lett., 102, 181101
Aleksić J. et al., 2015, J. High Energy Astrophys., 5, 30
Alves E. P., Zrake J., Fiuza F., 2018, Phys. Rev. Lett., 121, 245101
Balbus S. A., Hawley J. F., 1998, Rev. Mod. Phys., 70, 1
Beresnyak A., Lazarian A., 2008, ApJ, 682, 1070
Beresnyak A., Lazarian A., 2009, ApJ, 702, 460
Beresnyak A., Lazarian A., 2010, ApJ, 722, L110
Boldyrev S., 2006, Phys. Rev. Lett., 96, 115002
Boldyrev S., Perez J. C., 2009, Phys. Rev. Lett., 103, 225001
Boldyrev S., Perez J. C., Borovsky J. E., Podesta J. J., 2011, ApJ, 741, L19
Cerutti B., Werner G. R., Uzdensky D. A., Begelman M. C., 2013, ApJ, 770, 147
Chandran B. D. G., 2000, Phys. Rev. Lett., 85, 4656
Chandran B. D. G., 2008, ApJ, 685, 646
Chandran B. D. G., Foucart F., Tchekhovskoy A., 2018, J. Plasma Phys., 84, 905840310
Chen C. H. K., 2016, J. Plasma Phys., 82, 535820602
Chen C. H. K., Bale S. D., Salem C. S., Maruca B. A., 2013, ApJ, 770, 125
Cho J., Kim H., 2016, J. Geophys. Res., 121, 6157
Cho J., Lazarian A., 2014, ApJ, 780, 30
Comisso L., Sironi L., 2018, Phys. Rev. Lett., 121, 255101
Comisso L., Sironi L., 2019, ApJ, 886, 122
Davelaar J., Philippov A. A., Bromberg O., Singh C. B., 2020, ApJ, 896, L31

Demidem C., Lemoine M., Casse F., 2020, Phys. Rev. D, 102, 023003

Elsasser W. M., 1950, Phys. Rev., 79, 183
Galtier S., Nazarenko S. V., Newell A. C., Pouquet A., 2000, J. Plasma Phys., 63, 447
Gogoberidze G., Voitenko Y. M., 2020, Ap&SS, 365, 149
Goldreich P., Sridhar S., 1995, ApJ, 438, 763
Grošelj D., Mallet A., Loureiro N. F., Jenko F., 2018, Phys. Rev. Lett., 120, 105101
Hester J. J., 2008, ARA&A, 46, 127
Hoshino M., 2013, ApJ, 773, 118
Iroshnikov P. S., 1964, Sov. Astron., 7, 566
Kim H., Cho J., 2015, ApJ, 801, 75
Kraichnan R. H., 1965, Phys. Fluids, 8, 1385
Kunz M. W., Stone J. M., Quataert E., 2016, Phys. Rev. Lett., 117, 235101
Lithwick Y., Goldreich P., 2001, ApJ, 562, 279
Lithwick Y., Goldreich P., Sridhar S., 2007, ApJ, 655, 269
Mason J., Perez J. C., Boldyrev S., Cattaneo F., 2012, Phys. Plasmas, 19, 055902
Meyrand R., Squire J., Schekochihin A. A., Dorland W., 2021, J. Plasma Phys., 87, 535870301
Miloshevich G., Passot T., Sulem P. L., 2020, ApJ, 888, L7
Passot T., Sulem P. L., 2019, J. Plasma Phys., 85, 905850301
Perez J. C., Boldyrev S., 2009, Phys. Rev. Lett., 102, 025003
Perez J. C., Boldyrev S., 2010a, Phys. Plasmas, 17, 055903
Perez J. C., Boldyrev S., 2010b, ApJ, 710, L63
Perez J. C., Mason J., Boldyrev S., Cattaneo F., 2012, Phys. Rev. X, 2, 041005

Remillard R. A., McClintock J. E., 2006, ARA&A, 44, 49
Ripperda B. et al., 2021, J. Plasma Phys., 87, 905870512
Riquelme M. A., Quataert E., Sharma P., Spitkovsky A., 2012, ApJ, 755, 50
Schekochihin A. A., 2020, preprint (arXiv:2010.00699)
Schekochihin A. A., Cowley S. C., Dorland W., Hammett G. W., Howes G. G., Quataert E., Tatsuno T., 2009, ApJS, 182, 310
Schlickeiser R., 1989, ApJ, 336, 243
Shakura N. I., Sunyaev R. A., 1973, A&A, 500, 33
Sparks W. B., Biretta J. A., Macchetto F., 1996, ApJ, 473, 254
Takamoto M., Lazarian A., 2016, ApJ, 831, L11
Teaca B., Weidl M. S., Jenko F., Schlickeiser R., 2014, Phys. Rev. E, 90, 021101
TenBarge J. M., Howes G. G., Dorland W., Hammett G. W., 2014, Comput. Phys. Commun., 185, 578
TenBarge J. M. et al., 2021, preprint (arXiv:2105.01146)
Thompson C., Blaes O., 1998, Phys. Rev. D, 57, 3219
Towns J. et al., 2014, Comput. Sci. Eng., 16, 62
Voitenko Y., De Keyser J., 2016, ApJ, 832, L20
Wang Y., Boldyrev S., Perez J. C., 2011, ApJ, 740, L36
Wong K., Zhdankin V., Uzdensky D. A., Werner G. R., Begelman M. C., 2020, ApJ, 893, L7
Zhdankin V., 2021, preprint (arXiv:2106.00743)
Zhdankin V., Werner G. R., Uzdensky D. A., Begelman M. C., 2017, Phys. Rev. Lett., 118, 055103
Zhdankin V., Uzdensky D. A., Werner G. R., Begelman M. C., 2018a, MNRAS, 474, 2514
Zhdankin V., Uzdensky D. A., Werner G. R., Begelman M. C., 2018b, ApJ, 867, L18
Zhdankin V., Uzdensky D. A., Werner G. R., Begelman M. C., 2019, Phys. Rev. Lett., 122, 055101

APPENDIX A: DEPENDENCE ON DOMAIN SIZE

If the ratio $L/2\pi\rho_{e0}$ is small, the small separation between the characteristic scale of kinetic effects and the system size scale could influence the results presented in Section 3. In this appendix, we examine the box-size dependence of representative quantities for extremal values of the balance parameter $\xi = 0.0$ and $\xi = 1.0$ and for $L/2\pi\rho_{e0} \in \{27.1, 40.7, 54.3, 81.5\}$, corresponding to $N \in \{256, 384, 512, 768\}$. These results also include three very large simulations of balanced turbulence from Zhdankin et al. (2018b)
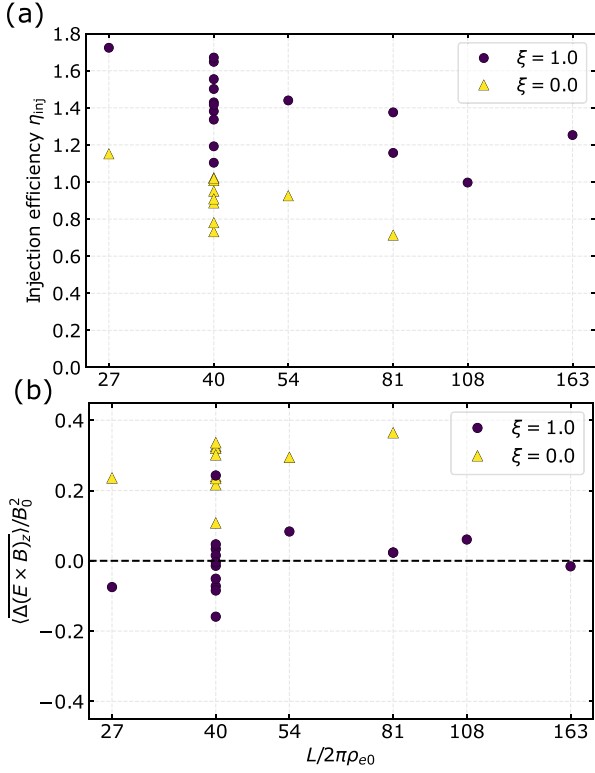
Figure A1. The injection efficiency and Poynting flux depend weakly on simulation domain size within statistical variation. When averaged from $t = 5-14\ L/c$, the injection efficiency (a) and Poynting flux along the background magnetic field (b) are shown as a function of $L/2\pi\rho_{e0}$. Both the balanced ($\xi = 1.0$; purple circles) and most imbalanced values ($\xi = 0$; yellow triangles) are mostly within statistical variation of the $L/2\pi\rho_{e0} = 40.7$ sample of eight random seeds. The black dashed line indicates zero.

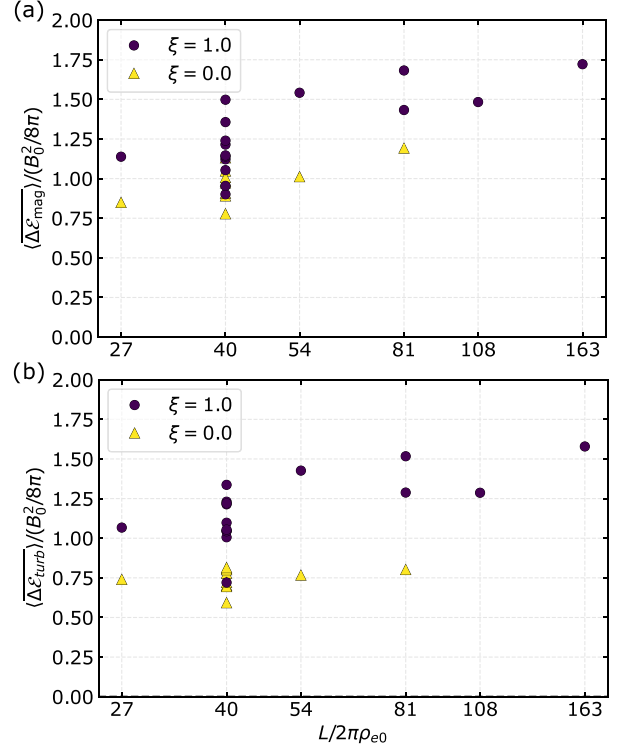averaged Poynting flux shows a weak positive trend with increasing

Figure A2. The magnetic and turbulent kinetic densities are weakly dependent on simulation domain size. When averaged from $t = 5 - 14\ L/c$, the magnetic energy density (a) and turbulent kinetic energy density (b) are shown as a function of $L/2\pi\rho_{e0}$. Both the balanced ($\xi = 1.0$; purple circles) and most imbalanced ($\xi = 0$; yellow triangles) values are mostly within statistical variation of the $L/2\pi\rho_{e0} = 40.7$ sample of eight random seeds.

with $L/2\pi\rho_{e0} \in \{81.5, 108.7, 164\}$ ($N = 768, 1024$, and 1536) that are otherwise identical to the other simulations of balanced turbulence. The time-averaging window has been changed from $10 < tc/L < 20$ to $5 < tc/L < 14$, because $14\ L/c$ is the latest time included in all simulations. Here we focus on the convergence of energetic quantities; for convergence of the balanced turbulence's particle energy spectra with system size, see Zhdankin et al. (2018b).

We find that the injection efficiency η_{inj} depends weakly on simulation domain size for both balanced and imbalanced turbulence (Fig. A1a). The simulations with $\xi = 1.0$ and $L/2\pi\rho_{e0} = 81.5$ and 164 domains have slightly lower injection efficiencies than those for the smallest ($L/2\pi\rho_{e0} = 40.7$) domains. Kinetic damping of large-scale fluctuations, which would drain energy faster than turbulence alone, may explain the larger η_{inj} for smaller domain sizes. For $\xi = 0$, the $L/2\pi\rho_{e0} = 54.3$ simulation's η_{inj} is within the statistical spread of the $L/2\pi\rho_{e0} = 40.7$ simulations' injection efficiencies, whereas the $L/2\pi\rho_{e0} = 81.5$ injection efficiency is slightly below. The time-

domain size (Fig. A1b). Though the $L/2\pi\rho_{e0} = 81.5$ domain size for the imbalanced $\xi = 0$ case has a value higher than the largest $L/2\pi\rho_{e0} = 40.7$ value, the difference is only about 0.05 ($cB_0^2/4\pi$) (about 15 per cent), within two standard deviations of the statistical variation shown by the $L/2\pi\rho_{e0} = 40.7$ study.

The turbulent and magnetic energy densities show a slight dependence on simulation domain size (Fig. A2). Both quantities' values for $L/2\pi\rho_{e0} \gtrsim 54.3$ are consistently about 15 per cent greater than the largest value of the statistical ensemble of $L/2\pi\rho_{e0} = 40.7$, $\xi = 1.0$ simulations. Though the imbalanced turbulence simulations do not appear to exhibit a trend in turbulent kinetic energy with box size (Fig. A2b), the $L/2\pi\rho_{e0} = 81.5$, $\xi = 0$ case's value for magnetic energy is noticeably higher (20 per cent) than the $L/2\pi\rho_{e0} = 54.3$ value, which lies within the statistical spread of the $L/2\pi\rho_{e0} = 40.7$ ensemble study (Fig. A2a).

This paper has been typeset from a TeX/LaTeX file prepared by the author.